Evolutionary insights into T-type Ca^{2+} channel structure, function, and ion selectivity from the *Trichoplax adhaerens* homologue

Carolyn L. Smith,[1]* Salsabil Abdallah,[2]* Yuen Yan Wong,[2]* Phuong Le,[2]* Alicia N. Harracksingh,[2] Liana Artinian,[3] Arianna N. Tamvacakis,[3] Vincent Rehder,[3] Thomas S. Reese,[1] and Adriano Senatore[2]

[1]National Institute of Neurological Diseases and Stroke, National Institutes of Health, Bethesda, MD 20892
[2]University of Toronto Mississauga, Mississauga, Ontario L5L 1C6, Canada
[3]Georgia State University, Atlanta, GA 30302

Four-domain voltage-gated Ca^{2+} (Ca_v) channels play fundamental roles in the nervous system, but little is known about when or how their unique properties and cellular roles evolved. Of the three types of metazoan Ca_v channels, Ca_v1 (L-type), Ca_v2 (P/Q-, N- and R-type) and Ca_v3 (T-type), Ca_v3 channels are optimized for regulating cellular excitability because of their fast kinetics and low activation voltages. These same properties permit Ca_v3 channels to drive low-threshold exocytosis in select neurons and neurosecretory cells. Here, we characterize the single T-type calcium channel from *Trichoplax adhaerens* (TCa_v3), an early diverging animal that lacks muscle, neurons, and synapses. Co-immunolocalization using antibodies against TCa_v3 and neurosecretory cell marker complexin labeled gland cells, which are hypothesized to play roles in paracrine signaling. Cloning and in vitro expression of TCa_v3 reveals that, despite roughly 600 million years of divergence from other T-type channels, it bears the defining structural and biophysical features of the Ca_v3 family. We also characterize the channel's cation permeation properties and find that its pore is less selective for Ca^{2+} over Na^+ compared with the human homologue $Ca_v3.1$, yet it exhibits a similar potent block of inward Na^+ current by low external Ca^{2+} concentrations (i.e., the Ca^{2+} block effect). A comparison of the permeability features of TCa_v3 with other cloned channels suggests that Ca^{2+} block is a locus of evolutionary change in T-type channel cation permeation properties and that mammalian channels distinguish themselves from invertebrate ones by bearing both stronger Ca^{2+} block and higher Ca^{2+} selectivity. TCa_v3 is the most divergent metazoan T-type calcium channel and thus provides an evolutionary perspective on Ca_v3 channel structure–function properties, ion selectivity, and cellular physiology.

INTRODUCTION

Voltage-gated calcium (Ca_v) channels play fundamental roles in the physiology of neurons and muscle, by coupling electrical signals carried largely by voltage-gated sodium (Na_v) and potassium (K_v) channels, with intracellular Ca^{2+}-dependent processes (Clapham, 2007). Of the three classes of Ca_v channels, L-type/Ca_v1 channels are central for excitation-contraction coupling in muscle and excitation-transcription coupling in neurons and muscle, whereas N- and P-/Q-type (i.e., Ca_v2) channels are central for fast presynaptic excitation-secretion coupling (Catterall, 2011). T-type/Ca_v3 channels serve less obvious functions (Perez-Reyes, 2003; Senatore et al., 2012), but one clear contribution is their role in regulating cellular excitability, where their low voltages of activation and fast kinetics permit rapid depolarizing Ca^{2+} currents below the action potential threshold. T-type channels also play roles in driving low threshold exocytosis in both vertebrates and invertebrates, and in mammals have been shown to directly interact with presynaptic components of the vesicular SNARE complex (Weiss et al., 2012; Weiss and Zamponi, 2013). Notably, recent genomic studies indicate that T-type channels, and in fact the majority of genes with important roles in the nervous system, are present in primitive animals that lack nervous systems and single-celled organisms that predate animals (King et al., 2008; Srivastava et al., 2008, 2010; Steinmetz et al., 2012; Moran et al., 2015; Moroz and Kohn, 2015). We know little, however, about the function and properties of these extant gene homologues or about the functional or proteomic adaptations that were required to incorporate their primordial counterparts into nervous system function.

One very intriguing early diverging animal is *Trichoplax adhaerens* (phylum Placozoa), which has only six cell types and lacks synaptically connected neurons and muscle (Schierwater, 2005; Smith et al., 2014). Despite these absences, *Trichoplax* is able to coordinate motile behavior such as feeding (Smith et al., 2015), chemotaxis, and phototaxis (Heyland et al., 2014), indicative of trans-cellular signaling and communication independent of both chemical and electrical synapses. Given that Ca_v channels play crucial roles in both intra- and

*C.L. Smith, S. Abdallah, Y.Y. Wong, and P. Le contributed equally to this paper. Correspondence to Adriano Senatore: adriano.senatore@utoronto.ca

Abbreviations used: AID, α interaction domain; EGFP, enhanced green fluorescent protein; ML, maximum likelihood; RT, reverse transcription.

The Rockefeller University Press $30.00
J. Gen. Physiol. 2017 Vol. 149 No. 4 483–510
https://doi.org/10.1085/jgp.201611683

intercellular signaling, it is intriguing that the *Trichoplax* genome bears a full complement of Ca_v channel genes: Ca_v1, Ca_v2, and Ca_v3 (Srivastava et al., 2008).

Here, we sought to characterize the molecular properties of the most basal metazoan homologue of T-type channels from *T. adhaerens*. Co-immunolocalization of the channel, named TCa_v3, with neurosecretory cell marker complexin labeled gland cells, shown previously to resemble neurosecretory cells in their expression of SNARE proteins and the presence of membrane-apposed vesicles (Syed and Schierwater, 2002; Smith et al., 2014). We cloned and in vitro expressed TCa_v3, finding that despite its ancient divergence, it bears the hallmark structural and biophysical features of T-type channels, including a low voltage of activation, rapid and transient kinetics, and an apparent Ca^{2+} window current near resting membrane potential.

We also characterized the permeation properties of TCa_v3, finding that the channel conducts moderately mixed inward Ca^{2+}-Na^+ currents, with a majority of current carried by Ca^{2+}, similar to mammalian homologues (Shcheglovitov et al., 2007). Paradoxically, measuring Ca^{2+} over Na^+ selectivity using bi-ionic reversal potential analysis (i.e., where inward Ca^{2+} ions compete with outward Na^+ for permeation), revealed poor Ca^{2+} versus Na^+ selectivity compared with human $Ca_v3.1$, similar to the cloned T-type channel from invertebrate snail *Lymnaea stagnalis* (Senatore and Spafford, 2010; Senatore et al., 2014). We attribute the relatively low Na^+ permeation through TCa_v3, in spite of its poor Ca^{2+} over Na^+ selectivity, to retention of a potent Ca^{2+} block. Based on comparative data, we suggest that Ca^{2+} block is more crucial for determining the degree of Na^+ that permeates alongside Ca^{2+} compared with pore selectivity and is a locus for evolutionary change in T-type channel cation permeability.

MATERIALS AND METHODS

Cloning of the TCa_v3 channel cDNA

Two cDNA libraries were made from *Trichoplax* whole-animal total RNA, one with an anchored oligo-dT_{18} primer, for PCR amplification and cloning of the C-terminal half of TCa_v3, and the other with a primer targeting a central region of the TCa_v3 coding sequence, for cloning the N terminus (Table 1). The TCa_v3 N- and C-terminal coding sequences were then independently amplified three times from the cDNA, via nested PCR using Pfu Turbo DNA polymerase (Agilent Technologies), with nested N- and C-terminal primer pairs containing NheI–XhoI and XhoI–XmaI sites, respectively. The nested NT primer (TCa_v3 NT 5′2) also contained a mammalian Kozak translation initiation site (Kozak, 1986; i.e., 5′-GCCACC-3′; Table 1) for effective expression of the TCa_v3 channel protein in mammalian cells. PCR-amplified DNA fragments were subcloned into pIRES2-IR–enhanced green fluorescent protein (EGFP), sequenced, and compared with each other plus the *Trichoplax* genome (JGI Genome Portal, Grell-BS-1999 v1.0, scaffold_2:6781672-6793175) to generate a consensus coding sequence. The full-length TCa_v3 clone was then prepared by inserting the XhoI–XmaI C-terminal subclone into the pIRES2 vector bearing the N-terminal TCa_v3 fragment, producing pTCa$_v$3-IR-EGFP. The full-length consensus coding sequence of TCa_v3 was submitted to GenBank (accession no. KJ466205).

Table 1. **Sequence of primers used for cloning TCa_v3 cDNA and semiquantitative RT-PCR**

Primer	Sequence (5′ to 3′)
TCav3 NT cDNA	CTTTAGGTAGTATGAGCAAGGAATG
TCav3 CT cDNA	TTTTTTTTTTTTTTTTTVN
TCav3 NT 5′1	TGATGTTTTATTCAAGTCATGC
TCav3 NT 5′2	TACTTAGCTAGCCGCGGGAGCCACC**ATG**GATATTTCGTTC GCTATCAT
TCav3 NT 3′1	CATCAGGCGTCTTAACTTTGC
TCav3 NT 3′2	TGCTCTGTGGTGGATCTCGAG
TCav3 CT 3′1	CTTGATATTGATTAAATTTATCCAGATG
TCav3 CT 3′2	ACTCATCCCGGG**TTA**TACTAATGTTTGAATCAT
TCav3 CT 5′1	AAATCTGGTAGATCCTAATGAAGTC
TCav3 CT 5′2	TCGCGTTCCAATTGGTCCTCGAG
TCav1_F	AGTCTTTACCGATTTGGCTCTTCTTTG
TCav1_R	CAATTATACGACTGACACTCTTTCAAAGC
TCav2_F	CGTTTACAAAAGTCTGGATCAAGTTGCG
TCav2_R	CTGCTGTACATTTTGATATGTTAGTAAGATCATCTG
TCav3_F	GTAGAAGATCAGATGGAATTAACGGCTTCC
TCav3_R	TACTAATGTTTGAATCATTTTTCGAGGTAATGTGACC
TCavβ_F	AGTAATAAATTCTCAGGATTAGTGGAAGTGTCC
TCavβ_R	AACATCATTACGTTTTATTACTAGAGGATCTTG
TCavα2δ-a_F	CTCAAGCAGTGGACTAACTAAACTTTACC
TCavα2δ-a_R	CATAGCTGGTTATATGTCACAAATTCCTCTC
TCavα2δ-b_F	TTTACCACATCCTTCTTCAGCTTCTTGAC
TCavα2δ-b_R	AGCATACACTGATAGCTTTACATAGCG
TCavα2δ-c_F	GATATTCGAAATTTCGAATGATACCCTTTGC
TCavα2δ-c-R	CAACGCGAGAAGTAGAAGTGTCCG

Translation start and stop codons are in bold, and the Kozak sequences and restriction enzyme sites used for cloning are underlined.

Reverse transcription (RT)–PCR amplification of *Trichoplax* Ca_v channel and accessory subunit mRNAs

The *Trichoplax* genome encodes single gene homologues for each of the three metazoan Ca_v channel types (Ca_v1, Ca_v2, and Ca_v3; NCBI accession nos. XM_002108894.1, XM_002109739.1, and KJ466205, respectively), as well as a single $Ca_v\beta$ accessory subunit gene (XM_002110305.1) and three $Ca_v\alpha_2\delta$ Ca_v1/Ca_v2 accessory subunit genes ($Ca_v\alpha_2\delta a$, $Ca_v\alpha_2\delta b$, and $Ca_v\alpha_2\delta c$; NCBI accession nos. XM_002112625.1, XM_002112621.1, and XM_002111347.1). Primers were designed to amplify ~500-bp cDNA fragments of each of these genes by RT–PCR (Table 1), using a cDNA library prepared by RT (SuperScript III Reverse Transcription; Thermo Fisher Scientific) with an anchored oligo-dT_{18} primer (Table 1)

and whole-animal total RNA. PCR amplification was achieved in 25-µl reactions each containing 1.25 µl of 10 µM forward and reverse primers (Table 1); 0.125 µl of Taq DNA polymerase and 2.5 µl of corresponding 10× buffer (New England Biolabs, Inc.); 1 µl of 25 mM $MgCl_2$; 0.5 µl of 10 mM dNTP mix (New England Biolabs, Inc.); and 0.5 µl of cDNA template. Thermocycling conditions were 95°C for 2 min, 30 cycles of 94°C for 1 min, 59°C for 45 s, and 72°C for 1 min, and a final 10-min extension at 72°C.

Phylogenetic inference

Maximum likelihood (ML) phylogeny of various Ca_v channels was inferred from a MUSCLE-alignment of select channel protein sequences (Edgar, 2004), generated with the program MEGA7 (Kumar et al., 2016). Alignments were timed with trimAl (Capella-Gutiérrez et al., 2009), followed by some minor manual trimming to remove highly heterogeneous regions (raw sequences and the trimmed alignment are provided in FASTA format as Supplementary Files 1 and 2, respectively). ML model selection was achieved with MEGA7, revealing that the LG+G model was most suitable under both the corrected Akaike's information criterion (AICc) and the Bayesian information criterion (BIC). The ML phylogenetic tree presented in Fig. 1 B was thus inferred from the trimmed alignment using the LG+G model, with 1,000 bootstrap replicates to generate node support values. Protein accession numbers used in the analysis are as follows: *Amphimedon* Ca_v1/Ca_v2, Aqu2.38198_001 from published transcriptome (Fernandez-Valverde et al., 2015); *Salpingoeca* Ca_v1/Ca_v2, XP_004989719.1; *Salpingoeca* Ca_v3, XP_004995501.1; *Trichoplax* Ca_v1 and Ca_v2, unpublished transcriptome; *Trichoplax* Ca_v3, KJ466205; *Nematostella* Ca_v1, XP_001639054.1; *Nematostella* Ca_v2a, Ca_v2b, and Ca_v2c, NVE4667, NVE18768, and NVE1263, respectively, from published transcriptome (Fredman et al., 2013); *Nematostella* Ca_v3a and Ca_v3b, NVE5017 and NVE7616, respectively, from published transcriptome (Fredman et al., 2013); *Caenorhabditis elegans* Ca_v1 (egl-19), NP_001023079.1; *C. elegans* Ca_v2 (unc-2), NP_001123176.1; *C. elegans* Ca_v3 (cca-1), CCD68017.1; *Drosophila* Ca_v1 (α1-D), AAF53504.1; *Drosophila* Ca_v2 (cacophony), AFH07350.1; *Drosophila* Ca_v3 (Ca-α1T), ABW09342.1; *Lymnaea* Ca_v1, AAO83839.1; *Lymnaea* Ca_v2, AAO83841.1; *Lymnaea* Ca_v3, AAO83843.2; human $Ca_v1.1$, NP_000060.2; human $Ca_v1.2$, Q13936.4; human $Ca_v1.3$, NP_001122312.1; human $Ca_v1.4$, NP_005174.2; human $Ca_v2.1$, O00555.2; human $Ca_v2.2$, NP_000709.1; human $Ca_v2.3$, NP_001192222.1; human $Ca_v3.1$, NP_061496.2; human $Ca_v3.2$, NP_066921.2; human $Ca_v3.3$, NP_066919.2; *Mnemiopsis* Ca_v2, fragmented transcriptome sequences manually pieced together from published transcriptome (Ryan et al., 2013); *Hormiphora* Ca_v2, sequence extracted from a de novo assembly of RNA-Seq data (SRR1992642; Francis et al., 2015); *Chlamydomonas* CAV2, XP_001701475.1; *Schizosaccharomyces pombe* CCH1, NP_593894.1; and *Saccharomyces cerevisiae* CCH1, NP_011733.3.

Immunostaining and confocal microscopy

Trichoplax were frozen and freeze-substituted as described previously (Smith et al., 2014) with the following modifications. Coverslips (22 mm square, #1.5 thickness; ZEISS) were cleaned in nitric acid and treated with 3-aminopropyltriethoxysilane (#A3648; Sigma-Aldrich) to produce a positively charged surface. *Trichoplax* were transferred to a 500-µl drop of artificial seawater (ASW) placed in the center of the coverslips and left to adhere for 1–2 h. 300 µl of the ASW was removed and replaced with 500 µl of a 1:1 mixture of ASW and 1 M mannitol. After ∼5 min, the liquid was removed, and the coverslips were plunged into tetrahydrofuran at −80°C on dry ice and kept overnight. The coverslips were transferred to methanol with 1.6% paraformaldehyde on dry ice and then held at −20°C for 2–3 h and room temperature for 2 h. The specimens were rinsed in 100% ethanol (EtOH) and rehydrated gradually with 90%, 70%, and 50% EtOH (diluted with PBS) and PBS each for ∼10 min and blocking buffer (BB: 3% normal goat serum, 2% horse serum, 1% BSA in PBS) for 15 min. Then specimens were incubated in custom (Thermo Fisher Scientific) antiserum against the epitope ESRVNGNAKFTSDDQ RLDR corresponding to the middle of the TCa_v3 I–II cytoplasmic linker (Fig. 1 A) or, to control for specificity, serum from the same rabbit before immunization both diluted 1:400 in BB overnight at 4°C. A custom (New England Peptide) chicken antibody against the epitope EATAPKKDSSKSNFSSR, found in the *Trichoplax* complexin protein, was added in some experiments to mark neurosecretory cells. After washing in PBS, the coverslips were incubated with Atto 488 goat anti–rabbit IgG (62197; Sigma-Aldrich) with/without Alexa Fluor 647 goat anti–chicken IgY (A-21449; Thermo Fisher Scientific) diluted 1:500 in BB for 2 h at room temperature. Nuclei were stained with Hoechst.

Images of immunostaining in *Trichoplax* were captured on an LSM 880 confocal microscope (ZEISS) with a 63× 1.4-N.A. PlanApo objective and 488-nm illumination for Atto 488 and 405-nm for Hoechst. Overview image stacks (17 images, 0.7-µm interval) were captured with a Quasar spectral detector with emission windows at 415–480 nm (blue) and 490–588 nm (green). Enhanced resolution image stacks (36 images, 0.185-µm interval) were collected with an Airyscan detector and 420–480- and 495–550-nm filters. Image stacks were displayed as maximum-intensity projections.

Immunodetection of TCa_v3 on Western blots

Trichoplax whole-animal protein lysates were prepared from ∼30 specimens and lysed directly in 200 µl of re-

ducing sample buffer preheated to 95°C (50 mM dithiothreitol, 1% wt/vol SDS, 7.5% glycerol, 0.003% bromophenol blue, and 40 mM Tris pH 6.8). Protein lysates from ectopically expressed TCa_v3 channels in HEK-293T cells were prepared as follows. The entire coding sequence of TCa_v3 was excised from the pTCa$_v$3-IR-EGFP vector with restriction enzymes SacII and XmaI and cloned into pEGFP-C1 with the same sites (Takara Bio Inc.). The resulting plasmid pEGFP-TCa_v3, pTCa$_v$3-IR-EGFP, or the empty fusion vector pEGFP-C1 was cotransfected into HEK cells with rat $Ca_v\beta_{1b}$ and $Ca_v\alpha_2\delta_1$ subunits (as outlined in the culturing and transfection section of the Materials and methods below), and cells were incubated at 28°C for 4–5 d and then briefly washed with warm PBS (137 mM NaCl, 2.7 mM KCl, 10 mM Na_2HPO_4, and 1.8 mM KH_2PO_4, pH 7.4). Cells were then lysed with 600 µl of sample buffer (50 mM dithiothreitol, 1% wt/vol SDS, 7.5% glycerol, 0.003% bromophenol blue, and 40 mM Tris, pH 6.8). Equal volumes for each lysate were loaded on either freshly prepared 7.5% polyacrylamide gels or precast 4–20% polyacrylamide gradient gels (Invitrogen), and electrophoresis was performed in Invitrogen MES buffer using an XCell SureLock Mini-Cell Electrophoresis System (Invitrogen). For each experiment, paired gels were run: one was subjected to Coomassie staining to confirm equal protein content among samples, whereas the other was transferred to a nitrocellulose membrane using a Tris-glycine transfer buffer (25 mM Tris, 192 mM glycine, 20% vol/vol methanol, and 0.5% SDS, pH 8.3). Western blots performed using custom anti-TCa_v3 antibodies (rabbit polyclonal; Thermo Fisher Scientific) were done using (a) unpurified antibodies (terminal bleed serum, 1:1,000 dilution); (b) preimmune serum (1:1,000 dilution); or (c) affinity-purified antibodies (isolated by the manufacturer using a conjugated antigen peptide, 1:500 dilution). Western blots against EGFP epitopes (as an N-terminal fusion with TCa_v3 or alone) were performed using a rabbit polyclonal anti-GFP antibody (Sigma-Aldrich) at 1:5,000 dilution. Primary antibody incubations were performed overnight at 4°C, and secondary antibody incubations, washing, and detection were performed using standard chemiluminescent methods.

Culturing and transfection of HEK-293T cells with TCa_v3 cDNAs

The detailed methods used for culture and $CaPO_4$ transfection of cloned Ca_v3 channels into HEK-293T cells, as well as techniques for whole-cell patch-clamp electrophysiology, have been previously documented in detail (Senatore et al., 2011, 2014; Senatore and Spafford, 2012). In brief, for electrophysiological experiments of in vitro–expressed TCa_v3, 6 µg of the pTCa$_v$3-IR-EGFP construct was transfected into HEK cells in 6-ml flasks, along with 3 µg of high voltage–activated calcium channel rat $Ca_v\beta_{1b}$ and $Ca_v\alpha_2\delta_1$ subunit cDNAs cloned into mammalian expression vector pMT2 (Tomlinson et al., 1993). These Ca_v1/Ca_v2 subunits have been shown to not interact with or alter the biophysical properties of heterologously expressed mammalian and invertebrate T-type channels (Dubel et al., 2004; Dawson et al., 2014), but nevertheless boost membrane expression by some unknown mechanism (Dubel et al., 2004). $CaPO_4$ transfections were done overnight at 37°C, after which cells were washed and transferred to 28°C for 2–3 d before recording. On the day of recording, cells were trypsinized (Sigma-Aldrich) and plated onto glass coverslips, which were then transferred into 2-ml culture dishes with appropriate extracellular recoding solutions.

For experiments involving the quantification of EGFP fluorescence in transfected HEK cells, transfections were performed in quadruplicate, with 6 µg pTCa$_v$3-IR-EGFP, pEGFP-TCa_v3, or pEGFP-C1 cotransfected with 3-µg combinations of rat $Ca_v\beta_{1b}$ and $Ca_v\alpha_2\delta_1$ subunits or the empty mammalian expression vector pCDNA 3.1. After incubation at 28°C for 3 d, the cells were imaged with transmitted and fluorescent light at 100 magnification, using a ZEISS AxioCam MRm Rev3 camera mounted on an AxioObserver A1 inverted microscope. All flasks were imaged with the same exposure settings, ensuring that the brightest cells did not saturate the pixels during acquisition with ZEN Lite software (ZEISS). Integrated density of the acquired fluorescence images was measured using the ImageJ software (Schneider et al., 2012), and values were normalized against the highest value for each replicate set, averaged, and plotted.

Patch-clamp electrophysiology

We used previously documented electrophysiological recording solutions to characterize the biophysical properties of TCa_v3 in 2 mM Ca^{2+} saline (Figs. 7 and 8; Senatore and Spafford, 2012), assess the Ni^{2+} block (Fig. 9; Senatore and Spafford, 2010), compare Ca^{2+} versus Ba^{2+} conductance (Fig. 10, C and D; Senatore and Spafford, 2012), and assess divalent versus monovalent cation selectivity and permeability features (Fig. 10, A, B, E, and F; Figs. 11 and 12; and Fig. S3; Senatore et al., 2014). Whole-cell patch voltage clamp recordings were performed using an Axopatch 200B amplifier and a Digidata 1440A digitizer controlled with pCLAMP 10 software (Molecular Devices). Pipettes were pulled using a Sutter P-97 micropipette puller and heat polished such that pipette resistance in the bath ranged from 2 to 5 MΩ, with access resistance after membrane breakthrough between 4 and 10 MΩ. Series resistance was not compensated for because we only kept data with minimal access resistance and tight capacitive transients upon voltage step. Only recordings in which leak current was <10% of the peak inward current were used, and offline leak subtraction was done using Clampfit

software (Molecular Devices). Methods for Boltzmann transformation and curve fitting of electrophysiological data are described in previous publications (Senatore and Spafford, 2010, 2012). Relative permeabilities under bi-ionic conditions for TCa_v3 (i.e., P_{Ca}/P_X, where X = Li^+, Na^+, K^+, or Cs^+) were calculated using the bi-ionic Nernst equation (Hille, 2001) as described previously (Senatore et al., 2014). Statistical analyses comparing electrophysiology data for TCa_v3 with data from other in vitro–expressed channels were done using one-way analysis of variance (ANOVA); p-values are presented in Table 2, where we provide citations for data from other studies.

Online supplemental material

Fig. S1 shows the percentage minimum–maximum plot of the TCa_v3 channel protein coding sequence compared with the three human Ca_v3 channels ($hCa_v3.1$, $hCa_v3.2$, and $hCa_v3.3$). Fig. S2 is an alignment of the domain II P-loop of T-type channels corresponding to the exon 12 region. Fig. S3 shows superimposed current–voltage plots of various Ca_v3 channel homologues under different bi-ionic conditions. The Ca_v channel protein sequences used to generate the phylogenetic tree depicted in Fig. 1 B are provided in supplemental text file 1 (untrimmed, unaligned sequences) and supplemental text file 2 (trimmed, MUSCLE-aligned sequences), both in FASTA format.

RESULTS

Identification and sequencing of a Ca_v3 channel homologue from *T. adhaerens*

Various Ca_v3 channel protein sequences were blasted against the *T. adhaerens* genome (Srivastava et al., 2008; JGI Genome Portal), identifying a predicted *Trichoplax* T-type/Ca_v3 channel homologue (*T. adhaerens* Grell-BS-1999 v1.0, scaffold_2:6781672 -6793175). The predicted coding sequence served as a reference for RT-PCR amplification and sequencing of the *Trichoplax* Ca_v3 (TCa_v3) cDNA, amplified in two large fragments, with primers listed in Table 1. To build a consensus, every nucleotide along the 6,192-bp coding sequence of TCa_v3 was validated with a minimum of three independently amplified sequences. The resulting full-length open reading frame (submitted to GenBank with accession no. KJ466205) predicts a channel protein of 2,063 aa, a molecular mass of ∼238 kD, and a Kyte–Doolittle hydrophobicity profile with hydrophobic peaks corresponding to transmembrane helices (i.e., segments 1 to 6 or S1–S6) within each of IV repeat domains, conserved for all four-domain channels (Fig. 1 A). An inferred ML phylogeny of various Ca_v channel proteins places TCa_v3 basal to the two cnidarian T-type channels from *Nematostella vectensis* (Ca_v3a and Ca_v3b), as well as bilaterian protostome homologues *C. elegans* cca-1, *Drosophila* Ca-α1T, and *Lymnaea* LCa_v3, and chordate deuterostome homologues (human Ca_v3 isotypes $Ca_v3.1$-$Ca_v3.3$; Fig. 1 B). Recent phylogenomic studies have placed *Trichoplax* and its phylum (Placozoa) as a sister clade to the bilaterians and cnidarians, and sponges (phylum Porifera) and comb jellies (phylum Ctenophora) as the most early diverging animals (Srivastava et al., 2008, 2010; Ryan et al., 2013; Moroz et al., 2014; Pisani et al., 2015). Based on this phylogeny, *Trichoplax* is the earliest diverging animal to possess all three types of bilaterian/cnidarian Ca_v channels (i.e., Ca_v1, Ca_v2, and Ca_v3). Instead, the marine sponge/poriferan *Amphimedon queenslandica* and the two ctenophores *Mnemiopsis leidyi* and *Hormiphora californiensis* have only single Ca_v channel genes, forming either a clade with Ca_v2 types (i.e., ctenophores) or a sister clade with Ca_v1 and Ca_v2 types (i.e., *Amphimedon*, hence dubbed Ca_v1/Ca_v2-like; Moran and Zakon, 2014; Senatore et al., 2016). Interestingly, recent genome sequencing of choanoflagellate *Salpingoeca rosetta* revealed the presence of a T-type channel, indicating that Ca_v3 types likely predate Metazoa (Fig. 1 B; Fairclough et al., 2013; Moran and Zakon, 2014), and hence were lost in Porifera and Ctenophora. Thus, TCa_v3 is the most divergent homologue of vertebrate/human T-type channels identified to date in animals.

Of select Ca_v3 channels with validated mRNA sequences (i.e., TCa_v3, *C. elegans* Ca_v3 channel cca-1, human $Ca_v3.1$ to $Ca_v3.3$ isotypes, *L. stagnalis* Ca_v3, and *Drosophila melanogaster* Ca-α1T), the *Trichoplax* channel protein is among the smallest, with shorter cytoplasmic N- and C-terminal regions, as well as linkers between domains I–IV (Fig. 2 A). Instead, transmembrane regions (S1–S6 helices and corresponding linkers) are much more similar in length (Fig. 2 B), and indeed carry most of the protein sequence homology between different channels, whereas the cytoplasmic linkers and N/C termini exhibit much more divergence (Senatore and Spafford, 2010). The distant TCa_v3 bears what are perhaps the most distinguishing features of T-type channels: (a) a "selectivity filter" motif of EEDD, made up of negatively charged glutamate (E) and aspartate (D) residues that project into the pore to govern ion selectivity (Talavera and Nilius, 2006), distinct from the more calcium-selective EEEE selectivity filters of Ca_v1 and Ca_v2 channels (Figs. 1 A and 2 C); and (b) a predicted helix-loop-helix motif in the cytoplasmic linker between domains I and II, dubbed the "gating brake," which serves to prevent channel opening at hyperpolarized membrane voltages (Perez-Reyes, 2010a) and where mutations in human $Ca_v3.2$ are associated with childhood absence epilepsy (Figs. 1 A and 2 D; Arias-Olguín et al., 2008).

Table 2. **Comparison of mean biophysical and permeability parameters of in vitro expressed Ca_v3 channels (±SE; *n* values in parentheses)**

Parameter	TCa_v3	LCa_v3 (+8b-25c)	P-value	Ref.	$Ca_v3.1$	P-value	Ref.	$Ca_v3.2$	P-value	Ref.	$Ca_v3.3$	P-value	Ref.
Activation													
Peak of IV (mV)	−45	**−40**		1	−35		2	−35		2	***−25***		2
$V_{1/2}$	−59.32 ± 0.9 (8)	**−53.48 ± 0.34 (13)**	***	1	−49.3 ± 0.7 (26)	***	2	−48.4 ± 1.2 (10)	***	2	***−41.5 ± 1.1 (17)***	***	2
Slope (k, mV)	4.50 ± 0.25 (8)	5.46 ± 0.14 (13)	**	1	**4.6 ± 0.1 (26)**	NS	2	5.2 ± 0.4 (10)	NS	2	***6.2 ± 0.2 (17)***	***	2
Inactivation													
$V_{1/2}$	−74.15 ± 0.90 (10)	−70.89 ± 0.49 (16)	**	1	**−74.2 ± 1.1 (8)**	NS	2	−75.6 ± 0.7 (19)	NS	2	***−69.8 ± 0.9 (17)***	**	2
Slope (k, mV)	2.69 ± 0.11 (8)	**2.93 ± 0.08 (16)**	NS	1	5.5 ± 0.3 (8)	***	2	***6.2 ± 0.2 (19)***	***	2	6.1 ± 0.1 (17)	***	2
Activation kinetics													
τ (−50 mV)	14.36 ± 0.31 (8)	3.26 ± 0.13 (16)	***	1	8.2 ± 0.9 (8)	***	3	**9.9 ± 0.4 (10)**	***	3	***43 ± 3 (9)***	***	3
τ (−10 mV)	3.48 ± 0.13 (8)	0.74 ± 0.03 (16)	***	1	1.1 ± 0.1 (8)	***	3	**1.8 ± 0.1 (10)**	***	3	***5.9 ± 0.5 (9)***	***	3
Fold change	4.1	**4.4**			***7.5***			5.5			7.3		
Inactivation kinetics													
τ (−50 mV)	66.33 ± 3.39 (6)	27.51 ± 1.34 (16)	***	1	**62 ± 23 (8)**	NS	3	28 ± 3 (10)	***	3	***126 ± 22 (9)***	*	3
τ (−10 mV)	51.36 ± 1.53 (6)	15.67 ± 0.56 (16)	***	1	***16 ± 1 (8)***	***	3	15 ± 1 (10)	***	3	**80 ± 5 (9)**	***	3
Fold change	1.3	1.8			***3.9***			1.9			**1.6**		
Deactivation													
−100 mV	1.46 ± 0.06 (12)	**1.37 ± 0.05 (19)**	NS	1	2.6 ± 0.2 (9)	***	2	***3.6 ± 0.4 (14)***	***	2	1.12 ± 0.1 (31)	*	2
−70 mV	9.15 ± 0.66 (12)	2.28 ± 0.18 (19)	***	1	6.2 ± 0.4 (9)	**	2	**8.5 ± 1.1 (14)**	NS	2	***2.1 ± 0.1 (30)***	***	2
Recovery													
τ recovery (ms)	1275.05 ± 54.43 (6)	**908.04 ± 27.05 (14)**	***	1	***137 ± 5 (12)***	***	2	448 ± 36 (7)	***	2	260 ± 30 (18)	***	2
Nickel													
(IC_{50} μM)	335.0 ± 6.5 (9)	300.0 ± 29.2 (4)	NS	4	**304.8 ± 6.2 (5–6)**	*	5	***4.9 ± 2.0 (5–6)***	***	5	216 ± 9 (5-6)	***	5
Mixed Ca^{2+}/Na^{+} currents													
% increase in I_{max} (Ca^{2+})	42.09 ± 3.19 (8)	***12a: 1439.75 ± 82.50 (6)***	***	6	26.64 ± 9.24 (4)	*		31.96 ± 4.58 (11)	NS		**45.45 ± 7.59 (6)**	NS	
		12b: 153.02 ± 9.61 (7)	***	6									
% increase in I_{max} (Ba^{2+})	51.19 ± 2.64 (4)	***12a: 901.29 ± 120.33 (5)***	***	6	27.01 ± 3.17 (9)	***	6	36.88 ± 3.50 (7)	*	6	**49.91 ± 6.23 (4)**	NS	6
		12b: 121.07 ± 4.26 (3)	***	6									
Ca^{2+} vs. X^{+} permeability													
pCa/pLi	19.87 ± 1.30 (8)	**12a: 22.74 ± 0.41 (8)**	*	6	46.67 ± 2.32 (7)	***	6						
		12b: 27.40 ± 1.13 (7)	***	6									
pCa/pNa	35.61 ± 1.52 (8)	**12a: 33.06 ± 1.50 (6)**	NS	6	***89.56 ± 8.21 (6)***	***	6	80.58 ± 3.69 (4)	***		56.19 ± 2.99 (7)	***	
		12b: 41.49 ± 1.98 (8)	*	6									
pCa/pK	63.99 ± 4.19 (9)	**12a: 50.25 ± 1.56 (12)**	**	6	140.16 ± 12.02 (5)	***	6						
		12b: 78.93 ± 4.17 (11)	*	6									
pCa/pCs	114.83 ± 10.64 (7)	12a: 111.30 ± 8.57 (10)	NS	6	154.65 ± 7.99 (5)	*	6						
		12b: 113.76 ± 7.19 (11)	NS	6									

P-values for statistical comparisons for all channels with respect to TCa_v3 were generated using one-way ANOVA. *, $P < 0.05$; **, $P < 0.005$; ***, $P < 0.0005$; NS, not significantly different. Bold indicates the value most similar to TCa_v3, and bold italics indicates the value most different from TCa_v3. References: 1, Senatore and Spafford (2012); 2, Chemin et al. (2002); 3, Gomora et al. (2002); 4, Senatore and Spafford (2010); 5, Kang et al. (2006); 6, Senatore et al. (2014).

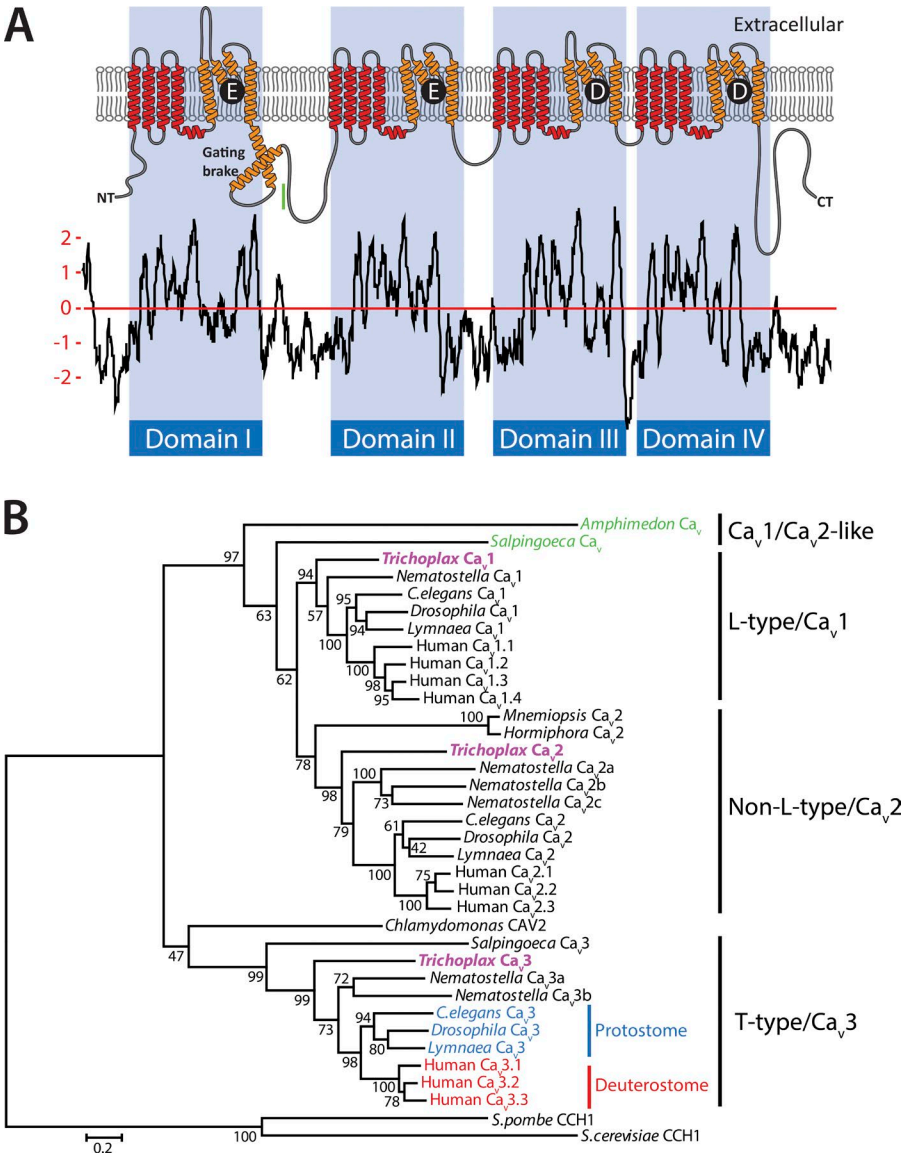

Figure 1. **Hydropathy profile of TCa$_v$3 and protein phylogeny of various Ca$_v$ channels.** (A) The in silico–translated protein sequence of TCa$_v$3 produces hydrophobic peaks on a Kyte–Doolittle hydrophobicity plot corresponding to six transmembrane helices (S1–S6) present in each of four homologous domains (I–IV), conforming to the characteristic structure of four-domain channels. The vertical green bar illustrates the location of the peptide epitope used to generate polyclonal anti-TCa$_v$3 antibodies. (B) Protein phylogeny of various Ca$_v$ channels, inferred by ML using the LG+G model. Node support values resulting from 1,000 bootstrap replicates are indicated, and the scale bar indicates the number of amino acid substitutions per site.

Reduced genomic complexity and absence of alternative splicing of the TCa$_v$3 gene

Most of the ~11,500 genes in the *Trichoplax* genome bear genomic architectures similar to orthologous genes in other animals (Srivastava et al., 2008). Accordingly, of the 28 exons/27 introns that make up the TCa$_v$3 channel gene, 26 splice junctions have counterparts in the Ca$_v$3.1 channel gene from mouse (*Mus*Ca$_v$3.1), whose mRNA transcript sequence is encoded by 38 exons/37 introns (Fig. 3). The *Trichoplax* Ca$_v$3 channel gene is ~10-fold shorter than *Mus*Ca$_v$3.1, attributable to much smaller intron sizes here and across the entire *Trichoplax* genome (Srivastava et al., 2008). To summarize major structural differences between the *Trichoplax* and mouse Ca$_v$3 genes (Fig. 3): (a) TCa$_v$3 lacks an intron separating exons 2 and 3, in the coding region for the domain I S1-S2 linker (Fig. 1 A), but retains N-terminal introns separating exons 1 and 2, as well as exons 3–4, 4–5, and 5–6, which are conserved in all metazoan four-domain channels including Ca$_v$ and Na$_v$ channels (Spafford et al., 1999); (b) TCa$_v$3 also lacks an intron separating exons 11 and 12 encoding the domain II extracellular P-loop between S5 and S6, which is found in all Ca$_v$3 channels stemming from basal bilaterians (Senatore et al., 2014); (c) TCa$_v$3 lacks alternative donor splice sites at the 3′ ends of exons 8 and 25, which in snail LCa$_v$3 and *Mus*Ca$_v$3.1 create optional exons 8b and 25c that regulate channel surface expression and gating, respectively (Chemin et al., 2001; Emerick et al., 2006; Shcheglovitov et al., 2008; Senatore and Spafford, 2012); (d) TCa$_v$3 lacks exon 26 found in all mammalian Ca$_v$3.1 and Ca$_v$3.2 channel genes, as well as *C. elegans* cca-1, which produces similar but more slight gating effects compared with exon 25c (Chemin et al., 2001; Ohkubo et al., 2005; Steger et al., 2005; Zhong et al., 2006; Senatore and Spafford, 2012); and (e) *TCa$_v$3* is missing four

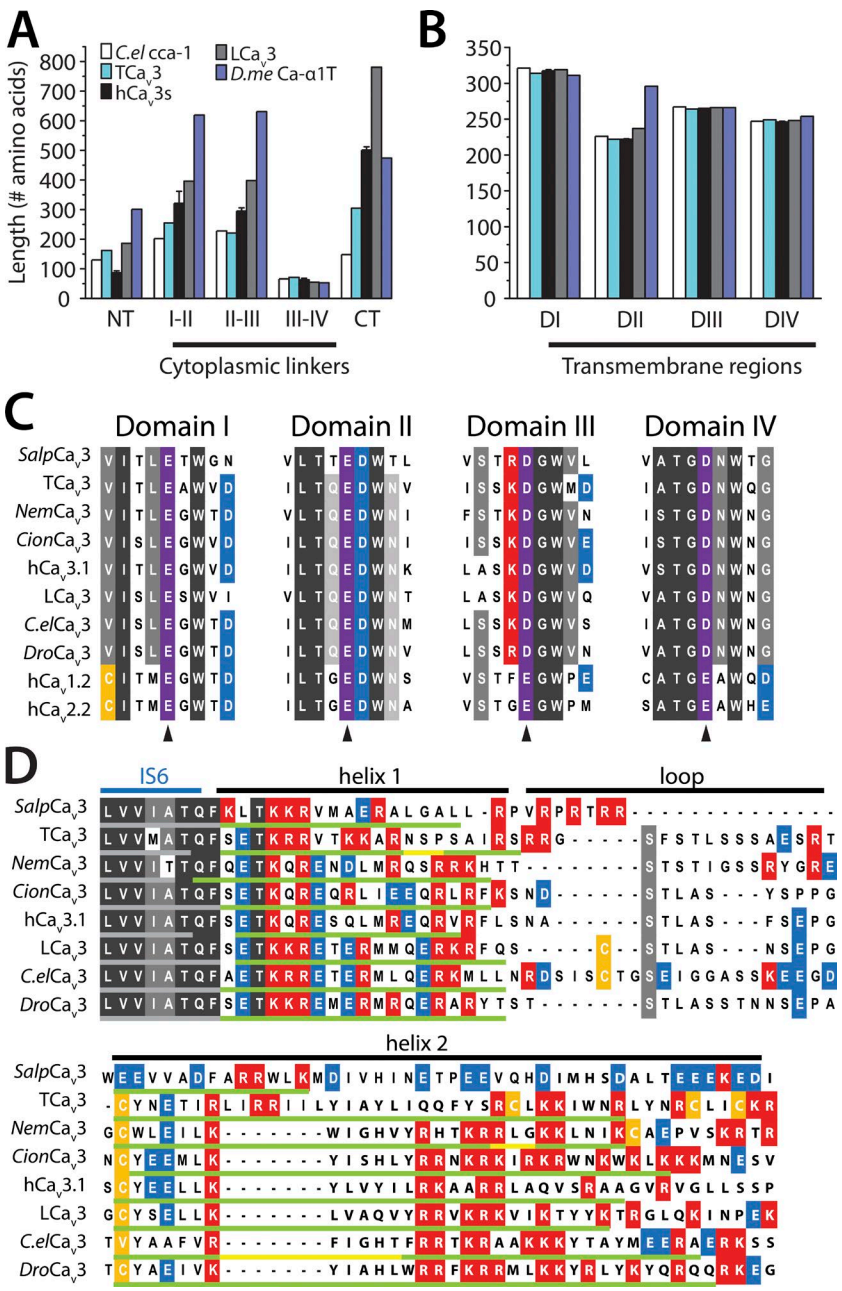

Figure 2. **Structural features of the TCa$_v$3 protein sequence compared to Ca$_v$1, Ca$_v$2, and Ca$_v$3 channels from other species.** (A) TCa$_v$3 has short N and C termini, as well as cytoplasmic linkers joining the four domains similar to the channel from *C. elegans* and much smaller, with the largest known T-type channels from *Lymnaea* and *Drosophila*. (B) Length of transmembrane regions and loops between segments 1 and 6 of each domain (D1–D4) are highly conserved for T-type channels, with domain I being the longest in amino acid length and domain II the shortest. Depicted values for the three human Ca$_v$3 channels (hCa$_v$3.1–hCa$_v$3.3) represent mean ± SE. (C) Alignment of Ca$_v$ channel selectivity filter and flanking amino acids, showing the conserved EEDD motif common to all Ca$_v$3 channels and distinct from the EEEE selectivity filters of high voltage–activated channels Ca$_v$1.2 and Ca$_v$2.2. (D) Prediction of secondary protein structure with PSIPRED (McGuffin et al., 2000) reveals a conserved helix-loop-helix gating brake motif in all T-type channels (green and yellow underlines depict predicted helices and regions where the prediction dropped below threshold, respectively) in the cytoplasmic I–II linker just proximal to the S6 pore-forming helix of domain I.

introns between exons 33 and 38 of *Mus*Ca$_v$3.1, corresponding to the channel C-terminal region. An overall reduction in genomic complexity for TCa$_v$3, especially in regions associated with alternative splicing, is consistent with reports that genes from basal metazoans generally undergo less alternative splicing (Pan et al., 2008; Wang et al., 2008; Gerstein et al., 2010; Graveley et al., 2011; Ramani et al., 2011). This was certainly evident during the sequencing and cloning of the TCa$_v$3 cDNA, in which we failed to identify a single alternatively spliced isoform, as well in an ongoing transcriptome analysis of *Trichoplax* whole-animal mRNAs (Senatore et al., 2016).

Adding to the analysis, Ca$_v$3 genes from premetazoan choanoflagellate *S. rosetta* and cnidarian *N. vectensis* reveal unique patterns in intron gain/loss across these different organismal lineages (Fig. 3). In keeping with the *Mus*Ca$_v$3.1 intro/exon numbering scheme, *Salp*Ca$_v$3 exon 8 is fused with flanking exons 7 and 9, which are conserved as separate exons in mouse and *Trichoplax*, and bears an additional three internal exons. Notably, this region encodes the channel I–II linker protein sequence (Fig. 1 A), which tends to be highly divergent between different Ca$_v$3 channels. In this equivalent position, *Nem*Ca$_v$3a has an additional exon compared with mouse and *Trichoplax*, which, interestingly, overlaps with mouse optional exon 8b, which alters channel membrane expression. *Salp*Ca$_v$3 notably lacks numerous introns between exons 12 and 33, a re-

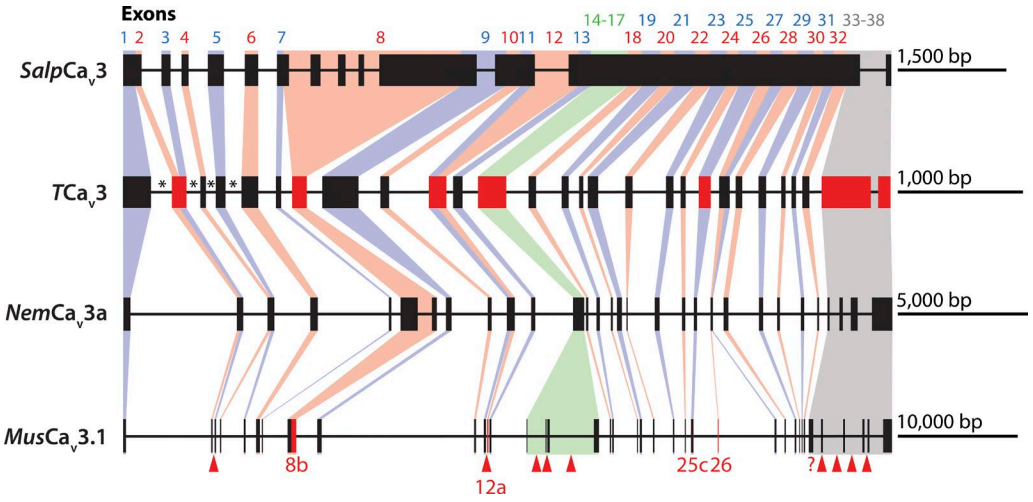

Figure 3. **Analysis of Ca$_v$3 channel genes from *S. rosetta* (*Salp*Ca$_v$3), *T. adhaerens* (TCa$_v$3), *N. vectensis* (TCa$_v$3), and *Mus musculus* (mouse; *Mus*Ca$_v$3.1).** Exons bearing start to stop codons are depicted by boxes, and introns are depicted by thin lines, with corresponding scale bars on the right indicating length in base pairs. Homologous protein sequences corresponding to mouse exons 1–38 are depicted by alternating blue and red background fills, with expanded mouse exons 14–17 colored in green and C-terminal exons 33–38 colored in gray. The TCa$_v$3 channel gene has a similar genomic structure as *Mus*Ca$_v$3.1; however, it is shorter in length (i.e., scale bars of 1,000 bp for TCa$_v$3 vs. 10,000 bp), and lacks nine introns (red arrowheads), resulting in 10 fewer exons (fused TCa$_v$3 exons are shown in red). TCa$_v$3 also lacks alternative splicing identified in channels from mammals and protostome invertebrates, including optional exons 8b, 25c, and 26, and mutually exclusive exons 12a and 12b (white arrow) found only in protostomes (red portions of the *Mus*Ca$_v$3.1 exons). Asterisks depict introns that are conserved among all metazoan four-domain channels.

gion encoding the C-terminal half of the channel protein (i.e., domains III and IV). Also evident is that *Mus*Ca$_v$3.1 exons 14–17 appear to have arisen via expansion from a single exon conserved in TCa$_v$3 and *Nem*Ca$_v$3a, in a region that corresponds the III–IV linker, which interestingly serves as a hotbed for modulation of mammalian T-type channels by kinases and G-proteins (Chemin et al., 2006; Perez-Reyes, 2010b; Senatore et al., 2012). Finally, *Nem*Ca$_v$3a and *Mus*Ca$_v$3.1 bear more exons/introns in the 3′ end of the gene, perhaps indicative of intron expansion in the cytoplasmic C terminus, a region with poor sequence homology where it is difficult to infer conserved intron/exon structure.

TCa$_v$3 is expressed in neurosecretory-like gland cells

Immunostaining *Trichoplax* with both crude and affinity-purified custom antibodies against a I–II linker epitope of TCa$_v$3 (site depicted in Fig. 1 A) outlined cells around the rim of the animal and, less intensely marked, scattered cells further in the interior (Fig. 4 A). Enhanced imaging with the Airyscan detector (1.7-fold improvement in resolution and improved signal-to-noise relative to conventional confocal [Huff, 2015]) revealed that TCa$_v$3 staining was near the surfaces of hourglass-shaped cells and concentrated at the side facing the exterior of the animal (Fig. 4 A, inset). Staining was not evident when using preimmune serum (Fig. 4 B). The cells that labeled for TCa$_v$3 also were stained by an antibody against *Trichoplax* complexin (Fig. 4 C), a regulator of SNARE secretory proteins in neurons. The distribution of the cells as well as their shapes closely matched those of gland cells labeled with antibodies against the SNARE proteins syntaxin-1, synaptobrevin, and SNAP-25 (Smith et al., 2014). No signal was apparent in specimens incubated with preimmune serum and imaged with the same parameters.

We also confirmed expression of TCa$_v$3 at the mRNA level by RT-PCR, where gene-specific primers amplified an appropriate ∼500-bp fragment from cDNA reverse transcribed from whole-animal total RNA using an oligo-dT$_{18}$ primer (Table 1 and Fig. 5). Similarly, primers targeting the other two *Trichoplax* Ca$_v$ channels, Ca$_v$1 and Ca$_v$2, as well as the Ca$_v$1/Ca$_v$2 accessory subunit Ca$_v$β and three Ca$_v$α$_2$δ subunits (Ca$_v$α$_2$δ-a, Ca$_v$α$_2$δ-b, and Ca$_v$α$_2$δ-c; Table 1), all produced expected bands of ∼500 bp, with no bands evident when the RTase enzyme was omitted from the reaction (Fig. 5). We also note that mRNA expression of these genes, as well as other genes homologous to those involved in cellular excitability (e.g., Na$_v$2 and K$_v$ channels, K$^+$ leak channels), are expressed in the whole-animal transcriptome of *Trichoplax* (Senatore et al., 2016).

Ectopic expression of TCa$_v$3 in HEK-293T cells

The TCa$_v$3 open reading frame (NCBI accession no. KJ466205) was cloned into bicistronic expression vector pIRES2-EGFP, which enables identification of positively transfected mammalian cells separately expressing TCa$_v$3 plus the fluorescent marker EGFP. Transfection of this construct (pTCa$_v$3-IR-EGFP) into HEK-293T

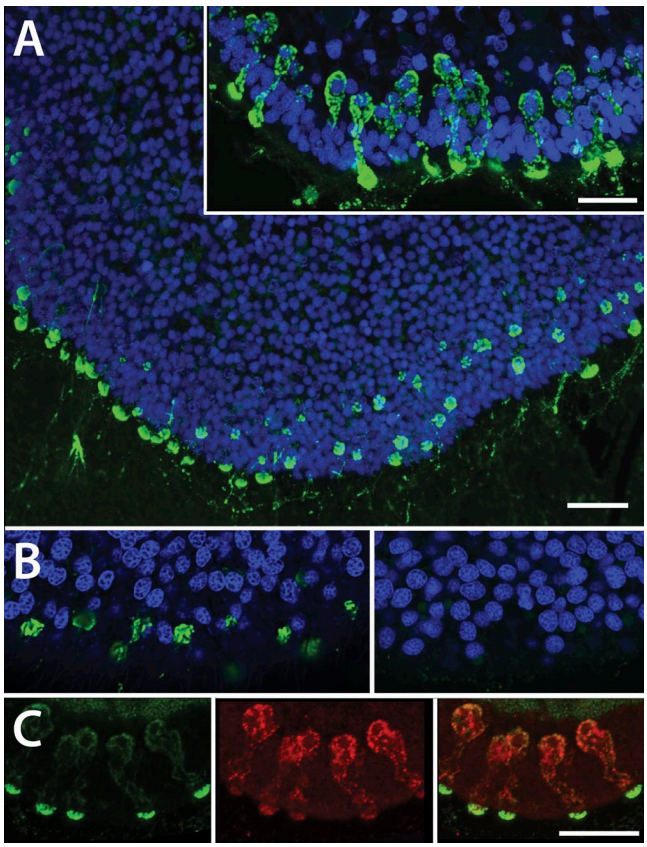

Figure 4. **Immunostaining for TCa$_v$3 in *Trichoplax* prepared by freezing and freeze substitution.** (A) Large field shows a projection of 17 optical sections extending through the dorsoventral thickness of the animal but omitting the dorsal and ventral surfaces where there is nonspecific staining. Labeled cells are concentrated around the rim but also present in the interior, although too dim to see in this unenhanced image. (Inset) Projection of 36 optical sections through cells reaching the ventral surface at the exterior of the animal. Staining is concentrated near the surfaces of hourglass-shaped cells and is most intense on the side facing the exterior. (B) Comparison of staining for TCa$_v$3 with matched preimmune control showing lack of staining for TCa$_v$3. (A and B) Nuclei are blue. (C) Cells that immunostain for TCa$_v$3 also label for complexin, a marker for neurosecretory cells. Merged view of double stain (right) shows TCa$_v$3 in green and complexin in red. The left panel shows TCa$_v$3 (green), and the middle panel shows complexin (red). A (inset) and C were collected with an enhanced detector (Airyscan). Bars: (A–C) 10 µm; (A, inset) 5 µm. The scale bar for B is shared with C.

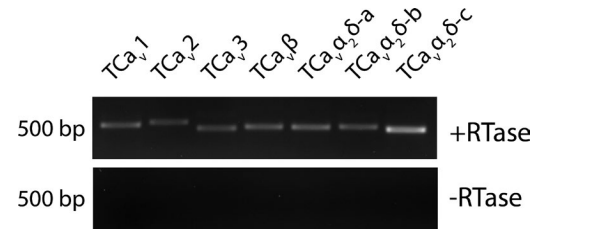

Figure 5. **RT-PCR amplification of various *Trichoplax* Ca$_v$ channel subunits.** RT-PCR amplification of cDNA corresponding to the three *Trichoplax* Ca$_v$ channels (TCa$_v$1, TCa$_v$2, and TCa$_v$3), the single Ca$_v$β subunit, and the three Ca$_v$α$_2$δ subunits (Ca$_v$α$_2$δ-a, Ca$_v$α$_2$δ-b, and Ca$_v$α$_2$δ-c) from a whole-animal total RNA cDNA library prepared with an anchored oligo-dT$_{18}$ primer.

cells produced barely detectable EGFP fluorescence (Fig. 6 A), suggesting that the TCa$_v$3 insert was somehow inhibiting expression of bicistronic EGFP because the empty pIRES2-EGFP vector normally produces robust EGFP fluorescence in these cells. Attempts to record voltage-activated Ca^{2+} currents from HEK cells transfected with pTCa$_v$3-IR-EGFP via whole-cell patch-clamp were unsuccessful, suggesting that the channel protein was also not expressed at high enough levels to accumulate at the cell membrane. A possible reason for the apparent poor expression of TCa$_v$3 is the prevalence of tandem rare codons in its cDNA sequence with respect to humans, which is expected to decrease efficiency of ectopic protein translation (Gustafsson et al., 2004; Kobayashi, 2015; Presnyak et al., 2015). Specifically, TCa$_v$3 exhibits a low codon adaptation index of 0.61 with respect to human preferred codons (Sharp and Li, 1987), and percentage minimum–maximum analysis reveals rare codon clustering along the entire length of the channel coding sequence (Fig. S1; Clarke and Clark, 2008).

Interestingly, previous research on cloned mammalian T-type channels revealed that coexpression with Ca$_v$β and Ca$_v$α$_2$δ accessory subunits of high voltage–activated Ca$_v$1 and Ca$_v$2 channels increases Ca$_v$3 channel expression by an indirect mechanism (Dubel et al., 2004). Thus, we sought to increase TCa$_v$3 channel expression in HEK cells by cotransfecting with rat Ca$_v$β$_{1b}$ and Ca$_v$α$_2$δ$_1$ subunit cDNAs cloned into the mammalian expression vector pMT2 (Tomlinson et al., 1993). Strikingly, cotransfection of pTCa$_v$3-IR-EGFP with rat Ca$_v$β$_{1b}$ and Ca$_v$α$_2$δ$_1$ subunit vectors produced an ∼217-fold increase in bicistronic EGFP fluorescence compared with cotransfection with empty mammalian expression vector pCDNA-3.1 (Fig. 6 A), quantified as relative integrated density with ImageJ software (Fig. 6 D). Cotransfection with just Ca$_v$β$_{1b}$ or Ca$_v$α$_2$δ$_1$ separately also increased fluorescence, but more moderately, with respective increases of ∼165-fold and 148-fold (Fig. 6 D). In addition, cotransfection of pTCa$_v$3-IR-EGFP with the rat Ca$_v$β$_{1b}$ and Ca$_v$α$_2$δ$_1$ subunits allowed us to electrophysiologically record robust TCa$_v$3 Ca^{2+} currents in HEK cells.

Because bicistronic expression and fluorescence of EGFP from pTCa$_v$3-IR-EGFP only indirectly implies TCa$_v$3 channel protein expression, we repeated the cotransfection experiment using a construct in which the channel coding sequence was cloned in frame with that of EGFP at the channel's N terminus, in the EGFP fusion vector pEGFP-C1. Cotransfection of the resulting pEGFP-TCa$_v$3 construct with rat Ca$_v$β$_1$b and Ca$_v$α$_2$δ$_1$ subunit vectors increased EGFP fluorescence ∼75-fold,

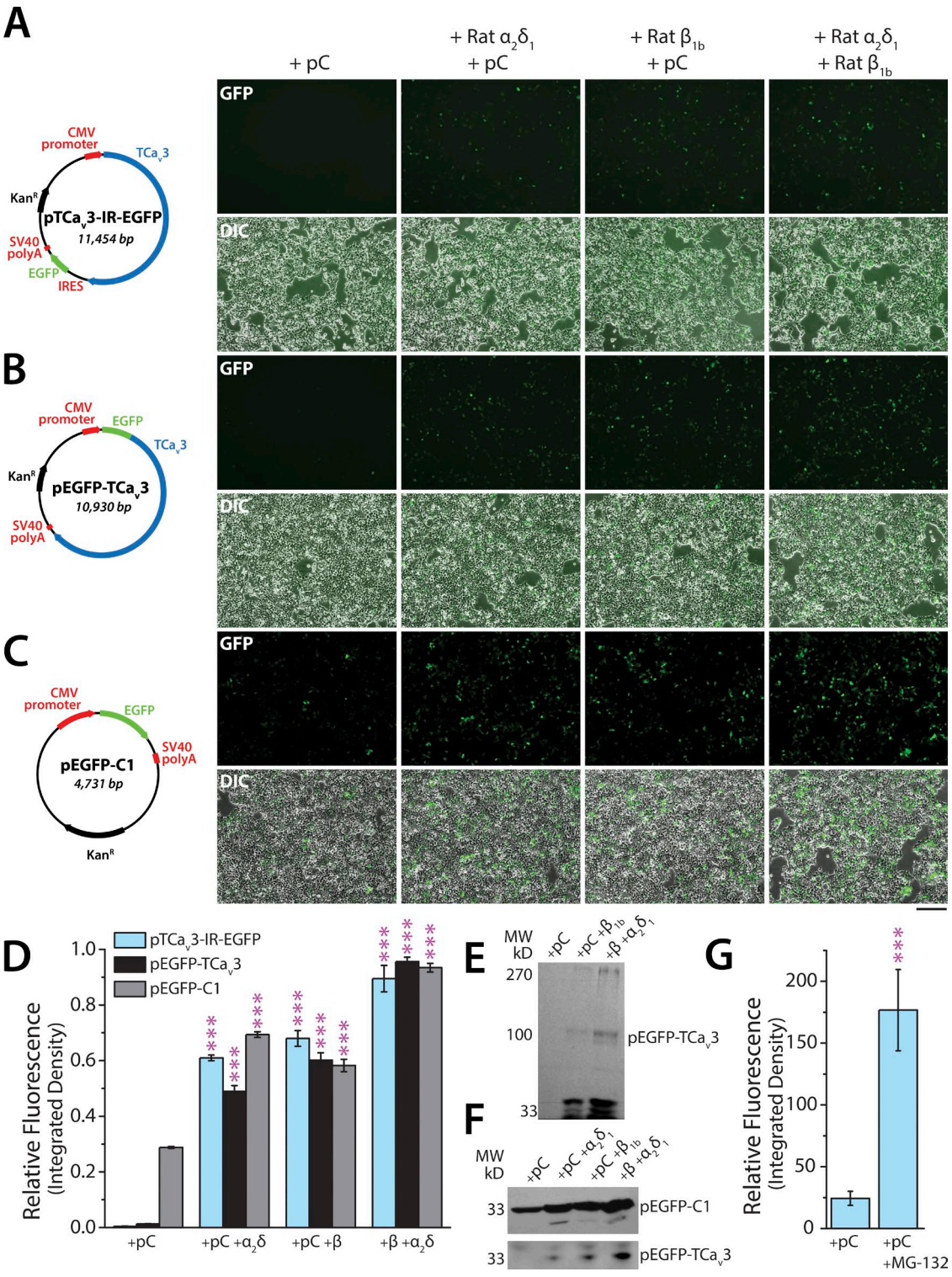

Figure 6. **In vitro expression of TCa_v3 in HEK-293T cells.** (A) Bicistronic EGFP fluorescence images (top) and merged EGFP/transmitted light images (bottom) of HEK-293T cells cotransfected with $pTCa_v3$-IR-EGFP (vector map on left) and pCDNA-3.1 (+pC) and/or pMT2 constructs bearing the coding sequences of rat $Ca_v\beta_{1b}$ and $Ca_v\alpha_2\delta_1$ accessory subunits. (B) Similar to A, but cells were transfected with the pEGFP-TCa_v3 construct, encoding a fusion protein of TCa_v3 tagged with N-terminal EGFP. (C) Similar to A, but cells were transfected with the empty EGFP fusion vector pEGFP-C1. Bar, 200 µm. (D) Bar graph depicting normalized mean fluorescence of imaged HEK cells from quadruplicate transfections (±SE). The purple asterisks denote statistically significant means (***, $P < 0.005$) comparing the +pC condition with all others via one-way ANOVA. (E) Western blot of HEK cell protein lysates with anti-EGFP antibody, prepared by cotransfection of the pEGFP-TCa_v3 vector with indicated combinations of pCDNA-3.1, rat $Ca_v\beta_{1b}$, and/or $Ca_v\alpha_2\delta_1$. (F) Western blot of HEK cell protein lysates with anti-EGFP antibody, prepared by cotransfection of the pEGFP-C1

whereas $Ca_v\beta_{1b}$ and $Ca_v\alpha_2\delta_1$ alone increased fluorescence ∼47-fold and ∼38-fold, respectively (Fig. 6, B and D). Interestingly, the $Ca_v\beta_{1b}$ and $Ca_v\alpha_2\delta_1$ vectors also increased fluorescence of EGFP when transfected without TCa_v3, from the empty vector pEGFP-C1 (Fig. 6, C and D), and this corresponded with increased EGFP protein levels apparent on Western blots of corresponding HEK cell lysates probed with anti-EGFP antibodies (Fig. 6 F).

We were unable to detect the endogenous TCa_v3 protein in Western blots of *Trichoplax* whole-animal lysates or blots of protein lysates from TCa_v3-transfected HEK cells when using the custom anti-TCa_v3 antibodies. Instead, blots of HEK cells transfected with pEGFP-TCa_v3 plus the $Ca_v\beta_{1b}$ and $Ca_v\alpha_2\delta_1$ vectors produced appropriate bands of ∼270 kD when probed with anti-EGFP (Fig. 6 E), consistent with the predicted molecular weight of the TCa_v3 channel protein (238 kD) plus EGFP (32.7 kD). In accordance with our inability to record TCa_v3 Ca^{2+} currents when pTCa$_v$3-IR-EGFP was transfected without the $Ca_v\beta_{1b}$ and $Ca_v\alpha_2\delta_1$ subunit vectors, we were unable to detect the EGFP-TCa_v3 fusion protein without cotransfection of $Ca_v\beta_{1b}$ and $Ca_v\alpha_2\delta_1$ (Fig. 6 E, left lane). Thus, the rat $Ca_v\beta_{1b}$ and $Ca_v\alpha_2\delta_1$ subunit vectors appear to dramatically boost protein expression of TCa_v3, as either an EGFP fusion protein or a separate protein from the pTCa$_v$3-IR-EGFP construct. However, the effect of $Ca_v\beta_{1b}$ and $Ca_v\alpha_2\delta_1$ subunit vectors on ectopic protein expression appears to be at least in part nonspecific because they also boost expression of coexpressed EGFP in the absence of TCa_v3 (Fig. 6, D and F).

Finally, in lanes on Western blots in which the subunits were included and EGFP-TCa_v3 protein expression was evident, several additional bands could be observed with molecular weights of ∼100 kD and a triplet of intense bands near 33 kD (Fig. 6, E and F), suggesting that the channel either is being degraded in HEK cells or is incompletely translated. Application of proteasome inhibitor MG-132 to cells transfected with pEGFP-TCa_v3 plus pCDNA-3.1 for 12 h before fluorescence imaging caused only a 7.2-fold increase in EGFP integrated density (Fig. 6 G), still below the detection limit of Western blotting (not depicted), suggesting that proteasomal degradation only partly accounts for the poor expression of TCa_v3. Notable is that coexpression of EGFP-TCa_v3 with the $Ca_v\beta_{1b}$ and $Ca_v\alpha_2\delta_1$ subunits does not appear to increase channel protein expression by decreasing the amount of degradation, but rather, by increasing the total amount of protein, including the complete protein, plus all of the incomplete intermediates (Fig. 6, E and F).

TCa_v3 conducts low voltage–activated calcium currents in vitro, characteristic of T-type channels

Whole-cell voltage clamp recording of HEK cells cotransfected with pTCa$_v$3-IR-EGFP, rat $Ca_v\beta_{1b}$, and rat $Ca_v\alpha_2\delta_1$ produced low voltage–activated calcium currents in 2 mM external Ca^{2+} in response to depolarizing voltage steps from −110 mV to between −90 and 40 mV (Fig. 7 A). A plot of peak currents versus step potential (i.e., current–voltage or IV plot) reveals a slightly hyperpolarized maximal peak inward current of −45 mV (Fig. 7 B), which is between 5 and 20 mV more negative than that of other Ca_v3 channels (Table 2). Boltzmann transformation of the IV plot, which removes the influence of driving force to estimate the voltage dependence for channel activation, indicates that TCa_v3 activation begins at very low depolarizing potentials compared with published data for other Ca_v3 channels derived using similar methods (i.e., compare half-maximal activation [$V_{1/2}$] of −59.32 ± 0.9 mV for TCa_v3 vs. −53.48 ± 0.34 for *Lymnaea* Ca_v3 [Senatore and Spafford, 2012]; −49.3 ± 0.7 for human $Ca_v3.1$ [Chemin et al., 2002]; −48.4 ± 1.2 for $Ca_v3.2$ [Chemin et al., 2002]; and −41.5 ± 1.1 for human $Ca_v3.3$ [Chemin et al., 2002]), reaching maximal activation near −40 mV (Fig. 7 C and Table 2). Conversely, steady-state inactivation of TCa_v3, determined by measuring peak residual current after exposure to prolonged steady-state voltages (Fig. 7 C, inset), is quite similar for TCa_v3 with respect to other channels, especially $Ca_v3.1$ and $Ca_v3.2$ (i.e., $V_{1/2}$ for inactivation is −74.15 ± 0.90 for TCa_v3 and −74.2 ± 1.1 for human $Ca_v3.1$ [Chemin et al., 2002] and −75.6 ± 0.7 for human $Ca_v3.2$ [Chemin et al., 2002]; Table 2). Altogether, the voltage properties of TCa_v3 indicate that it is likely more active at threshold voltages compared with other Ca_v3 channels, where the channel is subject to roughly the same amount of inactivation, but is more readily activated by depolarization.

An important and characteristic feature of T-type channels are their "window" currents, which occur at steady-state voltages near rest through a pool of constitutively open channels (Dreyfus et al., 2010), providing a constant influx of Ca^{2+} that depolarizes the cell membrane to alter cellular excitability (Cain and Snutch, 2010) and increases cytosolic Ca^{2+} to regulate cell growth and proliferation (Lory et al., 2006; Taylor et al., 2008; Senatore et al., 2012; Gackière et al., 2013). Such

vector (top) or pEGFP-TCa_v3 (bottom) with the indicated combinations of pCDNA-3.1, rat $Ca_v\beta_{1b}$, and/or $Ca_v\alpha_2\delta_1$ accessory subunits. Note that the three smaller bands near 33 kD visible in E converge into one band in the lower panel because of an increase in the percentage of polyacrylamide from 7.5% to ∼20% in the gels used for Western blotting. (G) Bar graph depicting the mean increase (±SE) in integrated density of HEK cells transfected with pEGFP-TCa_v3 and pCDNA-3.1 upon the addition of proteasome inhibitor MG-132 to the cultured cells 12 h before imaging. The purple asterisks denote statistically significant means with ***, $P < 0.005$.

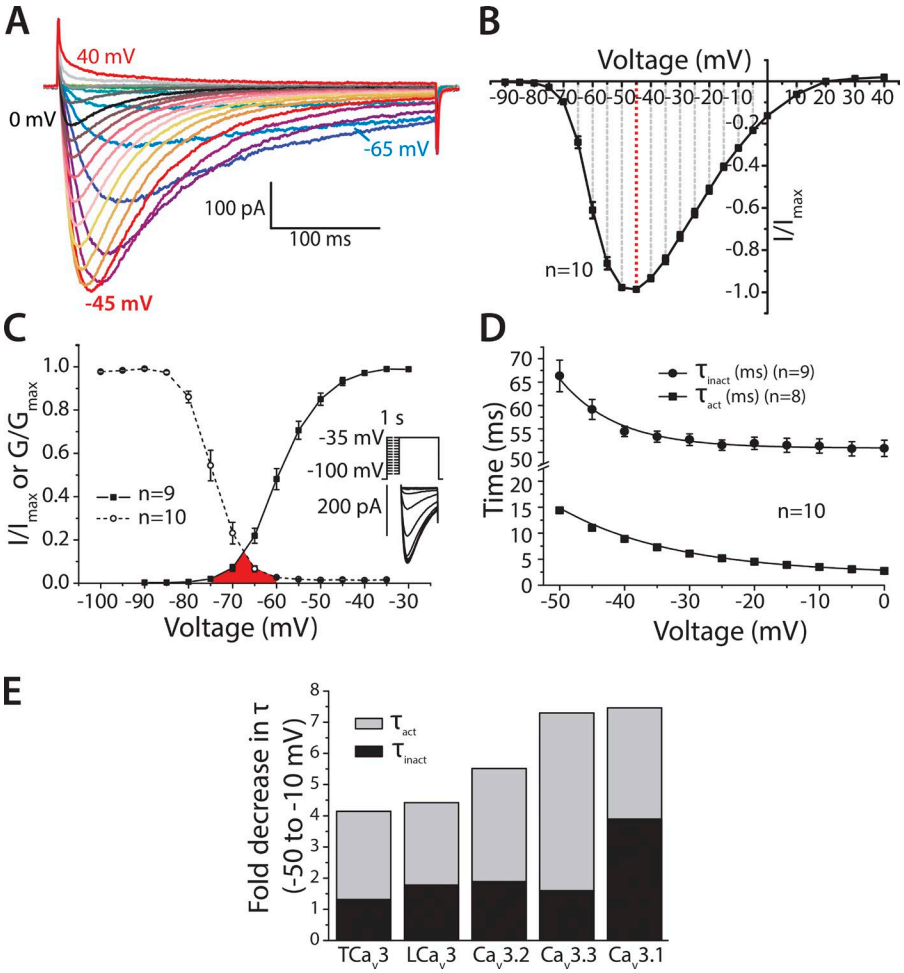

Figure 7. **Activation and inactivation properties of TCa$_v$3 Ca^{2+} currents.** (A) Sample traces of recorded Ca^{2+} currents conducted by the TCa$_v$3 channel ectopically expressed in HEK-293T cells, in response to depolarizing voltage steps from −110 mV to between −90 and 40 mV. The scale base below the current traces reflects time in milliseconds and current amplitude in picoamperes. (B) Plot of mean peak current for different depolarizing voltages, relative to the maximal peak inward current (i.e., an IV plot), reveals a maximal peak inward current at −45 mV, indicating a low voltage of activation for TCa$_v$3. (C) Plot of mean voltage dependence for channel activation (filled black squares, conductance G/G_{max}) and steady-state inactivation (white circles, I/I_{max}) reveals the presence of a window current for TCa$_v$3 (red fill). The inset shows the voltage protocol used to measure steady-state inactivation and sample elicited currents. (D) Mean τ values for mono-exponential curves fitted over the activation and inactivation phases of TCa$_v$3 macroscopic current waveforms reveals acceleration of channel kinetics upon stronger depolarization, measured as τ_{act} and τ_{inact}, respectively. (E) TCa$_v$3 is at the lower end of the scale with respect to acceleration of kinetics from −50 to −10 mV, with less pronounced fold decreases in τ_{act} and τ_{inact} compared with other in vitro–expressed channels, indicative of attenuated voltage dependency for activation and inactivation kinetics. Error bars indicate SE.

a window current is evident for TCa$_v$3, for which an overlap between channel activation and inactivation reveals a voltage range between −60 and −75 mV, where not all channels are inactivated and some degree of activation takes place (Fig. 7 C, red fill).

Kinetic properties of TCa$_v$3 macroscopic currents are also characteristic of T-type channels

In vitro TCa$_v$3 currents exhibit slow onset (activation) and attenuation (inactivation) at slight depolarizing voltage steps, which accelerate with stronger depolarization "tightening" current waveforms, a hallmark of Ca$_v$3 channels that produces a crossing over of inactivation curves toward peak inward current (Fig. 7 A). Such changes in current waveforms can be quantified with time constants (τ) for mono-exponential curve fits over the rise ($\tau_{activation}$) and decay ($\tau_{inactivation}$) phases of channel currents, which for TCa$_v$3 results in a decrease in τ consistent with accelerating kinetics upon stronger depolarization (Fig. 7 D). The rate at which TCa$_v$3 activation accelerates through depolarization is lower compared with other in vitro–expressed channels, with only a 4.13-fold drop in $\tau_{activation}$ from −50 to −10 mV versus 4.41-fold for *Lymnaea* Ca$_v$3 (Senatore and Spafford, 2010), 5.50-fold for human Ca$_v$3.2 (Gomora et al., 2002), 7.29-fold for human Ca$_v$3.3 (Gomora et al., 2002), and 7.45-fold for human Ca$_v$3.1 (Fig. 7 E and Table 2; Gomora et al., 2002). Likewise, acceleration of inactivation kinetics is slower, with only a 1.29-fold decrease in $\tau_{inactivation}$ for TCa$_v$3 versus 1.76-fold for LCa$_v$3, 1.87-fold for hCa$_v$3.2, 1.58-fold for hCa$_v$3.3, and 3.88-fold for hCa$_v$3.1 (Fig. 7 E and Table 2). From this data, it is clear that the two invertebrate channels compared here, TCa$_v$3 and the T-type channel from mollusk *L. stagnalis* (LCa$_v$3), have kinetics with an overall reduced voltage dependency, especially for current activation. TCa$_v$3 current kinetics are marginally slower across all negative voltages than other in vitro–expressed channels, with the exception of the slow Ca$_v$3.3 channel (Table 2).

Similar to *Lymnaea* Ca$_v$3, and in contrast to mammalian Ca$_v$3 channels, TCa$_v$3 recovers slowly from inactivation (Fig. 8, A and B; and Table 2), indicating that prolonged hyperpolarization would be required to ef-

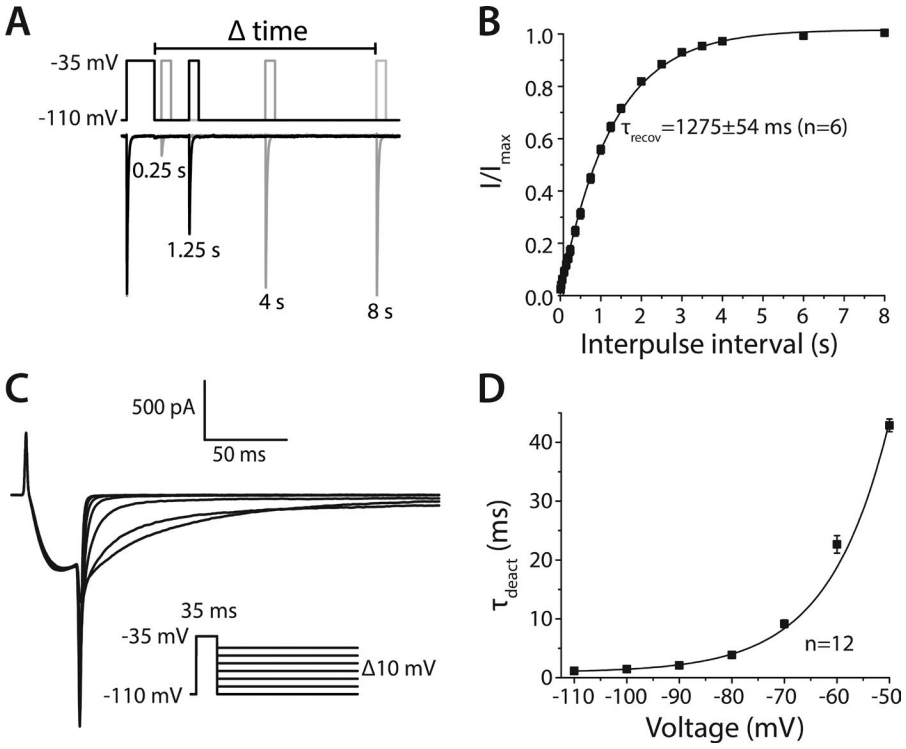

Figure 8. **Recovery from inactivation and deactivation properties of TCa_v3 Ca^{2+} currents.** (A) Illustration of the voltage protocol (top) used to measure recovery from inactivation for TCa_v3. A 1-s inactivating voltage pulse from −110 to −35 mV was followed by increasing interpulse interval durations of hyperpolarization at −110 mV to remove inactivation, followed by a short test pulse to −35 mV to record recovered peak inward Ca^{2+} current (sample traces, bottom). (B) Mean recovery from inactivation for TCa_v3 Ca^{2+} currents in HEK-293T cells, measured relative to the maximal peak inward current (I/I_{max}). A mono-exponential curve fitted over the data produces a τ time constant for recovered current (τ_{recov}) of 1,275 ± 54 ms. (C) Sample traces of TCa_v3 deactivation currents resulting from rapid membrane repolarization to different deactivating potentials while channels are fully open. The inset illustrates the voltage protocol used for deactivation. (D) τ values (τ_{deact}) for mono-exponential curve fitted over decaying inward currents at different deactivating voltages. Scale bars indicate time (milliseconds) and current amplitude (picoamperes). Plotted values in B and D represent mean ± SE.

fectively recruit the channel from depolarized membrane voltages. TCa_v3 also has slow deactivation kinetics relative to mammalian channels at voltages near −70 mV (Fig. 8, C and D; and Table 2), which during action potential repolarization would result in increased inward Ca^{2+} influx. Overall, despite the noted differences, the voltage dependencies and kinetics of TCa_v3 currents are remarkably similar to those of Ca_v3 channels from animals that have neurons and muscle (Table 2), in particular where a low voltage of activation and rapid activation and inactivation kinetics (which allow T-type channels to contribute depolarizing currents near action potential threshold) are conserved.

Ni^{2+} block of TCa_v3 Ca^{2+} currents

Early electrophysiological experiments revealed that the divalent cation Ni^{2+} could potently block low voltage–activated Ca^{2+} currents in some vertebrate preparations (Perez-Reyes, 2003). This high-affinity block was subsequently attributed only to the $Ca_v3.2$ channel isotype, and specifically to a unique histidine residue in its domain I S3–S4 extracellular loop (His-191) that strongly binds Ni^{2+} to disrupt channel gating (Fig. 9 A; Kang et al., 2006, 2010). The recently cloned T-type channel from *Drosophila* also bears a histidine in this loop (albeit 2 aa positions upstream of $Ca_v3.2$ His-191) and, not surprisingly, is also highly sensitive to Ni^{2+} (Jeong et al., 2015). Instead, TCa_v3, mammalian $Ca_v3.1$ and $Ca_v3.3$ channels, and *Lymnaea* LCa_v3, all lack histidines in this region (Fig. 9 A). Accordingly, all of these channels have low and remarkably similar IC_{50} values for Ni^{2+} block: 335.0 ± 6.5 µM for TCa_v3 (Fig. 9, B–D); 300.0 ± 29.2 for LCa_v3 (Senatore and Spafford, 2010); 304.8 ± 6.2 for human $Ca_v3.1$ (Kang et al., 2006); and 216 ± 9 for human $Ca_v3.3$ (Table 2; Kang et al., 2006). The similarity in IC_{50} values for all of these channels suggests that low-affinity Ni^{2+} block occurs through a common mechanism, where perhaps, as has been suggested for $Ca_v3.1$, extracellular Ni^{2+} ions bind two distinct regions of the pore in a cooperative manner (Obejero-Paz et al., 2008). Such a model is perhaps applicable to TCa_v3, where the Hill coefficient for Ni^{2+} block is greater than 1 (i.e., 1.18 ± 0.03; Fig. 9 D), suggesting some degree of cooperative binding. Interestingly, washout of Ni^{2+} is particularly fast for TCa_v3 compared with other T-type channels (Kang et al., 2006; Senatore and Spafford, 2010), with a transient increase in peak current amplitude (I/I_{max}) after perfusion of extracellular Ni^{2+} is replaced with Ni^{2+}-free saline (Fig. 9 C).

Ca^{2+} versus Na^+ permeation properties of TCa_v3

Recently, protostome invertebrates were found to uniquely possess alternative exons 12a and 12b, encoding alternate turret and descending helices of the domain II pore-loop (P-loop). In the freshwater mollusk

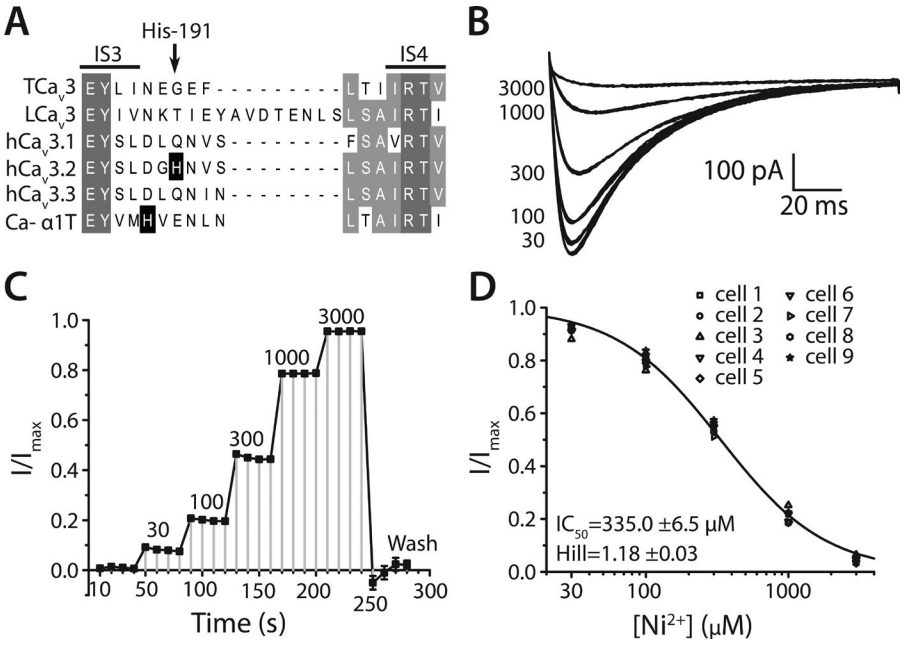

Figure 9. **Ni^{2+} block of TCa_v3 Ca^{2+} currents.** (A) Alignment of the domain I S3–S4 extracellular loop of various T-type channels, showing the presence of a key histidine residue in vertebrate (human) $Ca_v3.2$ associated with high sensitivity to Ni^{2+} block (His-191). *Drosophila* Ca-α1T is also highly Ni^{2+} sensitive and contains a histidine residue in this same loop 2 aa upstream of $Ca_v3.2$ His-191. (B) Sample peak Ca^{2+} currents through TCa_v3 resulting from increased concentrations of externally perfused Ni^{2+}. Applied Ni^{2+} concentrations, micromolar, are depicted on the left of the current waveforms. (C) Plot of sequential peak current responses of TCa_v3 as depicted in B resulting from the application of increasing concentrations of Ni^{2+} (mean ± SE; $n = 9$). Note the rapid washout of Ni^{2+} current inhibition and a transient augmented peak current the first few steps after washout. (D) Cumulative dose–response curve of TCa_v3 Ni^{2+} block, revealing an IC_{50} value of 335.0 ± 6.5 μM and a Hill coefficient of 1.18 ± 0.03.

L. stagnalis, these exons were found to produce channels with extremely bifurcated permeability features: whereas channels with exon 12b (i.e., LCa_v3-12b) conduct moderately mixed Ca^{2+}-Na^+ currents under physiological conditions, LCa_v3-12a is extremely Na^+ permeant, such that less than 10% of inward current is carried by Ca^{2+} (Senatore et al., 2014). Alignment of the domain II turrets of Ca_v3 channels from basal metazoans *Trichoplax* (TCa_v3) and *N. vectensis* (Ca_v3a) with channels from protostomes (i.e., *L. stagnalis*, *Drosophila*, and *C. elegans*), deuterostomes (*Ciona intestinalis*, human), and a premetazoan species (choanoflagellate *S. rosetta*) reveals that the TCa_v3 domain II P-loop resembles those of exon 12a–bearing channels, being smaller and containing fewer cysteines than exon 12b (Fig. S2).

We sought to assess whether the exon 12a–like turret of TCa_v3 is associated with moderate Na^+ permeability, similar to cnidarian (Lin and Spencer, 2001), mammalian (Shcheglovitov et al., 2007), and basal deuterostome (Hagiwara et al., 1975) channels, or instead associates with extreme Na^+ permeability, similar to exon 12a variants of *Lymnaea* Ca_v3. For this, we assessed the degree of mixing of Ca^{2+} and Na^+ currents through TCa_v3 ectopically expressed in HEK-293T cells by replacing a perfused extracellular recording solution containing 2 mM Ca^{2+} and 135 mM impermeant $NMDG^+$, with one containing Na^+ instead of $NMDG^+$ (Fig. 10, A and B). Addition of Na^+ resulted in a 42% increase in peak inward current elicited by stepping from −110 to −45 mV, which approximates the degree of Na^+ expected to move through the channel alongside Ca^{2+} upon membrane depolarization (Shcheglovitov et al., 2007; Senatore et al., 2014). Comparing the current increase of TCa_v3 with previously published data of other cloned channels (Senatore et al., 2014; Stephens et al., 2015) reveals that the *Trichoplax* T-type is most similar to the least Ca^{2+}-selective mammalian isotype $Ca_v3.3$ (i.e., 45%), whereas the exon 12b variant of LCa_v3 exhibits a larger increase of 153% in current amplitude and human $Ca_v3.1$ an increase of only 27%. In stark contrast, LCa_v3-12a undergoes a striking 1,440% increase in current amplitude upon perfusion of external Na^+ (Fig. 10 B), reflecting its dramatic Na^+ permeability. Thus, in the presence of Ca^{2+}, TCa_v3 appears to conduct only moderately mixed Ca^{2+}-Na^+ currents, in a range similar to that of other in vitro–expressed T-type channels, with the exception of the highly Na^+-permeant LCa_v3-12a.

Ca^{2+} versus Ba^{2+} permeability does not predict the amplitude of mixed divalent-monovalent cation currents through T-type channels

T-type channels are highly permeable to divalent cation Ba^{2+}, where for reasons that are unclear, the three rat Ca_v3 channel isotypes have dissimilarities with respect to macroscopic Ca^{2+} versus Ba^{2+}currents in vitro (Talavera and Nilius, 2006): $Ca_v3.1$ conducts larger Ca^{2+} currents, $Ca_v3.2$ conducts larger Ba^{2+} currents, and $Ca_v3.3$ conducts equal Ca^{2+} and Ba^{2+} currents (McRory et al., 2001). Here, we found TCa_v3 to be similar to rat $Ca_v3.1$, where replacing 2 mM external Ba^{2+} with equimolar Ca^{2+} by perfusion produced an increase in current amplitude upon membrane depolarization from −110 mV (Fig. 10 C), with a 2.29-fold increase in maximal peak

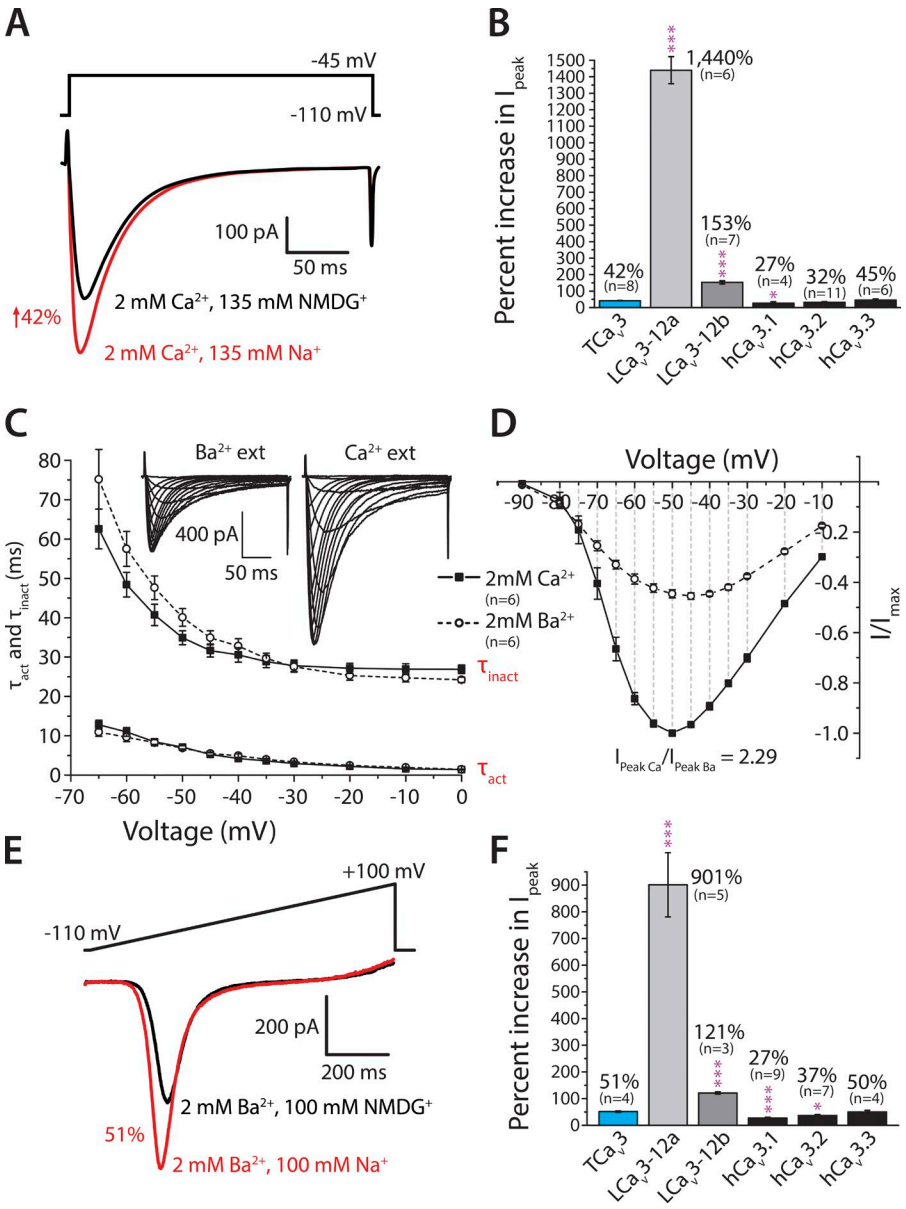

Figure 10. **TCa$_v$3 conducts moderately mixed Na$^+$/divalent cation currents in the presence of external Ca^{2+} or Ba^{2+}.** (A) Replacing 135 mM impermeant external cation NMDG$^+$ with Na$^+$, in the presence of invariant 2 mM Ca^{2+} produces a 42% increase in peak inward current through TCa$_v$3 elicited by a voltage step from −110 to −45 mV (black and red current traces, respectively), indicative of a moderate mixing of inward Ca^{2+} and Na$^+$ ions in macroscopic currents. (B) Mean percent increase in peak inward current at −45 mV (±SE), upon replacement of 135 mM external NMDG$^+$ with equimolar Na$^+$ in the presence of 2 mM external Ca^{2+}, for TCa$_v$3 compared with previously published data for other cloned Ca$_v$3 channels (Senatore et al., 2014; Stephens et al., 2015). (C) Macroscopic currents for TCa$_v$3 are larger in the presence of 2 mM external Ca^{2+} versus Ba^2 (inset), where mono-exponential curves fitted over activation and inactivation phases of the current waveforms (τ_{inact} and τ_{inact}, respectively) reveal statistically indistinguishable kinetics under one-way ANOVA. Plotted values represent mean ± SE. (D) Corresponding IV plots for mean peak Ca^{2+} versus Ba^{2+} currents (±SE) reveal a 2.29-fold increase in maximal peak inward current when Ca^{2+} is present in the extracellular solution instead of Ba^{2+}. (E) Replacing 100 mM impermeant external cation NMDG$^+$ with Na$^+$, in the presence of invariant 2 mM external Ba^{2+}, produces a 51% increase in peak inward current through TCa$_v$3 elicited by a voltage ramp from −110 to 100 mV (black and red current traces, respectively), indicative of a moderate mixing of Ba^{2+} and Na$^+$ ions in macroscopic currents. (F) Mean percent increase in peak inward current using the voltage ramp protocol (±SE), upon replacement of 135 mM external NMDG$^+$ with equimolar Na$^+$ in the presence of 2 mM external Ba^{2+}, for TCa$_v$3 compared with previously published data for other cloned Ca$_v$3 channels (Stephens et al., 2015). Asterisks depict statistical significance (p-values) for comparisons of means for increased inward current with Na$^+$ relative to TCa$_v$3 (generated by one-way ANOVA; *, P ≤ 0.05; ***, P ≤ 0.0005).

inward current visible on IV plots (Fig. 10 D). It appears as though the difference in macroscopic Ca^{2+} versus Ba^{2+} current amplitude for TCa$_v$3 is not attributable to differences in activation/inactivation kinetics in the presence of either ion, as was shown for rat Ca$_v$3.1 (Khan et al., 2008), where mono-exponential curves fitted over activation and inactivation phases of macroscopic currents for Ba^{2+} versus Ca^{2+} produce statistically indistinguishable τ time constants across all depolarizing voltages (Fig. 10 C). Interestingly, the *Lymnaea* T-type channel, which can alter its Ca^{2+} versus Na$^+$ permeation properties via alternative splicing of exons 12a and 12b, nevertheless always conducts approximately twofold larger Ba^{2+} than Ca^{2+} currents in vitro, regard-

less of exon 12 splicing (Senatore and Spafford, 2010; Senatore et al., 2014).

Differences in Ca^{2+} versus Ba^{2+} permeation among the various in vitro–expressed T-type channels have no consequence for the pattern in fold increases in peak inward current upon addition of external Na^+. Comparing the fold increase in peak macroscopic current through TCa_v3 elicited by ramping the voltage from −110 to 100 mV in the presence of 2 mM Ba^{2+} and either 100 mM Na^+ or $NMDG^+$ (Fig. 10 E) with previously published data from other in vitro–expressed channels (Senatore et al., 2014; Stephens et al., 2015) reveals a similar ranking in Na^+ permeation as observed in the presence of 2 mM external Ca^{2+}: LCa_v3-12a >> LCa_v3-12b > TCa_v3 ~ $hCa_v3.3$ > $hCa_v3.2$ > $hCa_v3.1$ (i.e., compare Fig. 10, B and F).

Ca^{2+} block of TCa_v3 Na^+ currents indicates high-affinity pore binding of external Ca^{2+}, similar to human $Ca_v3.1$

At extremely low concentrations of external Ca^{2+}, all Ca_v channels conduct prominent Na^+ currents. Titrating increasing concentrations of extracellular Ca^{2+} leads to a block of Na^+ current, with a sensitivity that reflects the affinity of Ca^{2+} to binding sites located in the pore. As $[Ca^{2+}]_{out}$ increases, the blocking effect reaches saturation levels, then Ca^{2+} itself becomes abundant enough to occupy multiple sites within the pore, leading to Ca^{2+} permeation (Tsien et al., 1987; Sather and McCleskey, 2003; Cheng et al., 2010; Buraei et al., 2014; Tang et al., 2014). This property, of a decrease in Na^+ current amplitude and a subsequent rise in Ca^{2+} current as $[Ca^{2+}]_{out}$ increases (known as the Ca^{2+} block effect), is exemplified by peak currents through human $Ca_v3.1$ elicited by repeating voltage steps from −110 to −35 mV, whereas external Ca^{2+} is perfused from 1 nM to 10 mM in the presence of invariant 60 mM external Na^+ (Fig. 11 A; Senatore et al., 2014). Notably, the TCa_v3 Ca^{2+}-block data are similar to previously published data for human $Ca_v3.1$ (Senatore et al., 2014; Stephens et al., 2015), where at 10 µM $[Ca^{2+}]_{out}$, 97.3% and 96.1% of peak Na^+ current elicited by voltage steps to −35 mV were blocked, respectively (Fig. 11, A and B). Human $Ca_v3.1$ Na^+ currents appear to be slightly more sensitive to Ca^{2+}, where at 0.1 µM $[Ca^{2+}]_{out}$, 34.1% of Na^+ current was blocked, whereas TCa_v3 and the two exon 12 variants of LCa_v3 only exhibit between −5.6 and 4.6% block. Beyond 10 µM $[Ca^{2+}]_{out}$, TCa_v3 and $Ca_v3.1$ show 13.8- and 9.4-fold increases in peak current caused by an emerging Ca^{2+} conductance (Fig. 11, A and C). In contrast, LCa_v3-12b shows a moderate reduction in Ca^{2+} block (82.6%), whereas the highly sodium-permeant LCa_v3-12a has a dramatically right-shifted dose–response for Ca^{2+} (Fig. 11 A), with only 44.5% of current blocked at 10 µM Ca^{2+} (Fig. 11 B; Senatore et al., 2014). Also noticeable is a continued decline in current amplitude beyond 10 µM $[Ca^{2+}]_{out}$ for the *Lymnaea* channel variants (Fig. 11 A), most marked for LCa_v3-12a, with a sevenfold continued decrease in current from 10 µM to 10 mM external Ca^{2+} (Fig. 11 C), further reflecting the reduced affinity for Ca^{2+} in the LCa_v3 pore. Collectively, the Ca^{2+} block data indicates that TCa_v3 exhibits a potent, but perhaps slightly diminished Ca^{2+}-block of Na^+ currents compared with human $Ca_v3.1$. Instead, the two exon 12 variants of *Lymnaea* Ca_v3 exhibit moderately attenuated and extremely attenuated Ca^{2+} block, indicative of lowered binding affinity for Ca^{2+} along the extracellular surface of the channel pore.

Ca^{2+} block, and not Ca^{2+} selectivity, determines the degree of Na^+ permeation through T-type channels

To further understand the Na^+ permeation properties of TCa_v3, we characterized its Ca^{2+} versus monovalent cation selectivity by measuring zero-current reversal potentials (E_{Rev}) under bi-ionic conditions (i.e., 4 mM Ca^{2+}_{out} and 100 mM Li^+_{in}, Na^+_{in}, K^+_{in}, or Cs^+_{in}). The reversal potential of peak bi-ionic currents is determined by the pore's preference for inward-permeating Ca^{2+}, which pulls E_{Rev} toward more positive voltages, versus outward-permeating monovalent cations (i.e., X^+, where X = Li, Na, K, or Cs), which pull E_{Rev} toward more negative voltages. Depolarizing voltage steps from −90 to 70 mV under the four bi-ionic conditions (i.e., Ca^{2+}_{out}-Li^+_{in}, Ca^{2+}_{out}-Na^+_{in}, Ca^{2+}_{out}-K^+_{in}, and Ca^{2+}_{out}-Cs^+_{in}) produce markedly different outward current components for TCa_v3, with decreasing amplitudes from Li^+ to Na^+ to K^+ to Cs^+ (Fig. 12 A), reflecting the pore's decreasing permeability to monovalent cation flow according to the Eisenman selectivity model (i.e., ions with smaller radii are more permeable through a narrow pore: $Li^+ < Na^+ < K^+ < Cs^+$ with respect to radius; Eisenman et al., 1967; Eisenman and Horn, 1983). Correspondingly, E_{Rev} values for the four bi-ionic IV plots for TCa_v3 have leftward shifts corresponding to increased monovalent permeation from Cs^+ to Li^+ (Fig. 12 B). Converting E_{Rev} values to permeability ratios P_{Ca}/P_X using the bi-ionic Nernst equation (Senatore et al., 2014), which reflect the pore's preference for Ca^{2+} over monovalent X^+, reveals that the *Trichoplax* channel is poorly selective for Ca^{2+} over X^+ monovalents compared with human $Ca_v3.1$ (Stephens et al., 2015), falling between previously published values for *Lymnaea* LCa_v3-12a and LCa_v3-12b variants for P_{Ca}/P_{Na} and P_{Ca}/P_K (Fig. 12 C; Senatore et al., 2014). Interestingly, TCa_v3 is the most Li^+-permeable channel, whereas the Cs^+ permeability for all non-deuterostome channels is roughly equal and significantly higher than human $Ca_v3.1$.

Ca^{2+} versus X^+ permeability features of T-type channels are also reflected in the rectification of macroscopic bi-ionic currents, where three conductance states are evident on IV plots: (1) an inward conductance at voltages where the driving force favors inward flow of Ca^{2+} (G_{In}); (2) a conductance through E_{Rev} where a

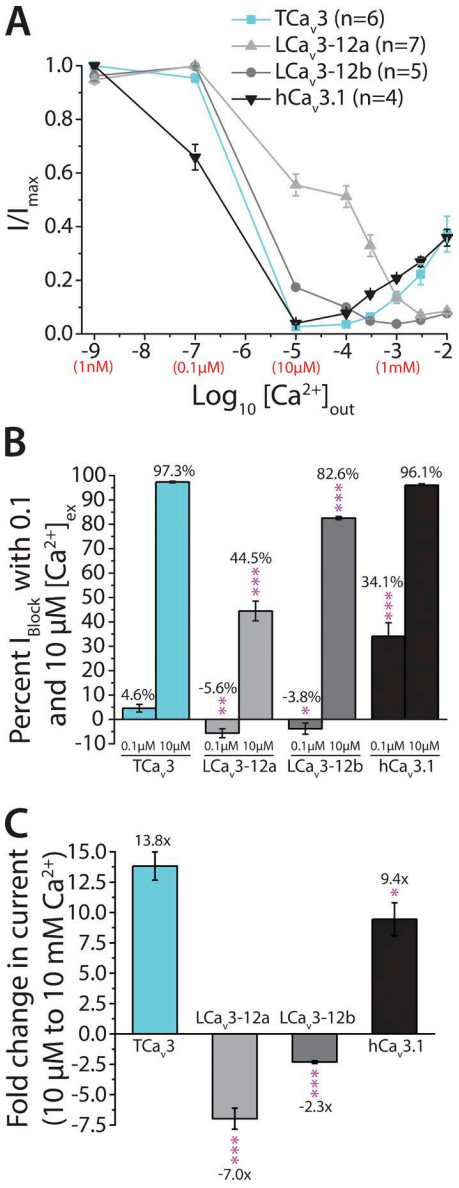

Figure 11. **Ca^{2+} block of inward Na$^+$ current for TCa$_v$3 compared with other cloned T-type channels.** (A) Ca^{2+} block of Na$^+$ currents for TCa$_v$3 compared with previously published data for human Ca$_v$3.1 and the two exon 12 splice variants of the *Lymnaea* channel, LCa$_v$3-12a and LCa$_v$3-12b (Senatore et al., 2014). Increasing external [Ca^{2+}] from 1 nM to 10 mM, in the presence of invariant external [Na$^+$] of 60 mM, blocks Na$^+$ currents through TCa$_v$3 with similar affinity as human Ca$_v$3.1, where at 10 μM external Ca^{2+} (i.e., 10^{-5} [Ca^{2+}]$_{out}$), mean peak inward currents (±SE) for Ca$_v$3.1and TCa$_v$3, elicited by voltage steps from −110 to −35 mV, show substantial attenuation from maximum (I/I$_{max}$). Instead, exon 12 variants of LCa$_v$3 show a reduced Ca^{2+} block, most dramatically for LCa$_v$3-12a. (B) Mean percent block of inward Na$^+$ currents (±SE) for the various Ca$_v$3 channels at 10 and 0.1 μM [Ca^{2+}]$_{out}$. Asterisks depict statistical significance (p-values) for comparisons of means for percent block relative to TCa$_v$3 (generated by one-way ANOVA; *, $P \leq 0.05$; **, $P \leq 0.005$; ***, $P \leq 0.0005$). (C) Mean fold increase/decrease in I/I$_{max}$ for the various cloned channels (±SE) as [Ca^{2+}]$_{out}$ is increased from 10 μM to 10 mM. Asterisks depict statistical significance (p-values) for comparisons of means for fold change in current relative to TCa$_v$3 (generated by one-way ANOVA; *, $P \leq 0.05$; ***, $P \leq 0.0005$).

transition between inward Ca^{2+} and outward X$^+$ occurs, (G_{Rev}); and (3) an outward conductance where driving force favors outward X$^+$ flow (G_{Out}; Fig. 12 D and Fig. S3). Comparison of the three conductance states of TCa$_v$3 with previously published data for other in vitro–expressed T-type channels (Senatore et al., 2014; Stephens et al., 2015) corroborates a low Ca^{2+} selectivity for the *Trichoplax* Ca$_v$3 channel compared with human Ca$_v$3.1. Both G_{Rev} and G_{Out} values for TCa$_v$3, which reflect permeability to monovalent cations, are significantly larger than those of Ca$_v$3.1, regardless of monovalent cation type (Fig. 12 E). Indeed, Ca$_v$3.1 is very ineffective at conducting outward monovalent currents, even at extremely depolarized potentials >60 mV (Fig. 12 D and Fig. S3). Ca$_v$3.1 also has the largest conductance for inward Ca^{2+} flow (G_{In}), but noticeably, under the most physiological conditions with K$^+$ present in the internal saline, the G_{In} Ca^{2+} conductance for TCa$_v$3 encroaches on that of Ca$_v$3.1 (i.e., means are not statistically different; Fig. 12 E). At the other extreme, the *Lymnaea* channel LCa$_v$3-12a has the lowest conductance for inward Ca^{2+} (G_{In}) and the largest monovalent conductances through E_{Rev} and outwards (G_{Rev} and G_{Out}, respectively; Fig. 12 D and Fig. S3). Collectively, the bi-ionic reversal potential data indicate that the TCa$_v$3 channel pore is poorly selective for Ca^{2+} over monovalents compared with human Ca$_v$3.1, with bi-ionic selectivity properties more similar to those of highly Na$^+$-permeant LCa$_v$3-12a and the more Ca^{2+}-selective LCa$_v$3-12b channels (Table 2).

In light of these data, it is apparent that Ca^{2+} block, and not Ca^{2+} selectivity, is the major determinant for the degree of Na$^+$ that permeates through TCa$_v$3 and other T-type channels. Indeed, the efficiency of Ca^{2+} block for the various cloned T-type channels (Ca$_v$3.1 > TCa$_v$3 > LCa$_v$3-12b > LCa$_v$3-12a; Fig. 11) correlates with their degree of Na$^+$ permeation (e.g., 21.0%, 29.6%, 60.5%, and 93.5% of total current carried by Na$^+$, respectively; measured by dividing percentage increases in peak current shown in Fig. 10 B by that same value plus 100%).

DISCUSSION

TCa$_v$3 is the most divergent metazoan T-type calcium channel

Ca$_v$3 channels appear to have emerged upwards of a billion years ago in a eukaryotic ancestor of choanoflagellates and metazoans (Morris, 1998), being present in the genome of *S. rosetta* (Fairclough et al., 2013; Moran and Zakon, 2014). We were unable to find a Ca$_v$3 channel homologue in the genome of choanoflagellate *Monosiga brevicollis* (King et al., 2008), indicative of either gene loss or an incomplete genome sequence. We also failed to identify Ca$_v$3 channel genes in various genomes and transcriptomes available for sponges and ctenophores (Srivastava et al., 2010; Ryan et al., 2013;

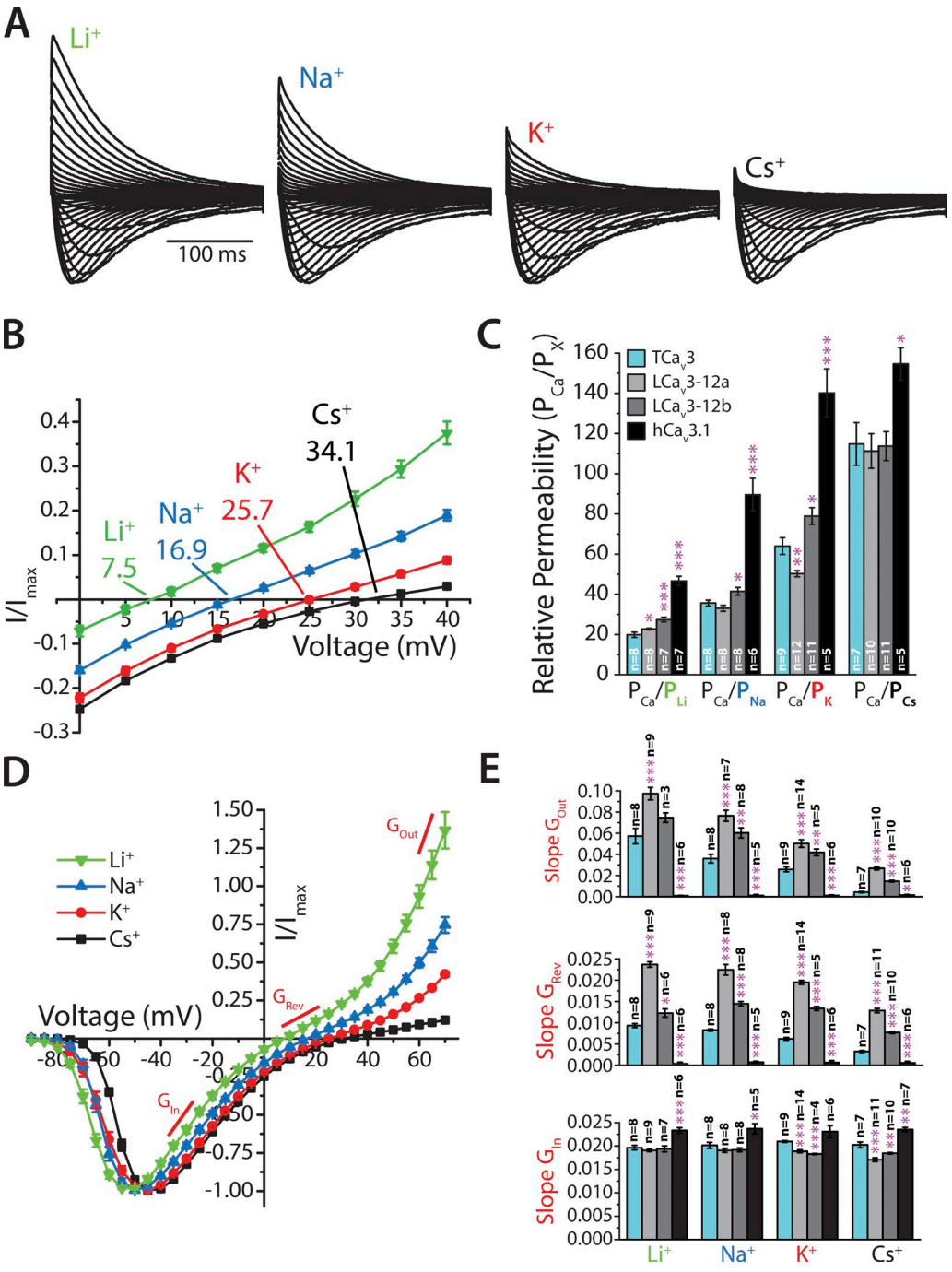

Figure 12. **Bi-ionic reversal potential analysis of TCa$_v$3 Ca^{2+} versus monovalent cation permeability and comparison with other cloned T-type channels.** (A) Sample current traces recorded for TCa$_v$3 recorded under different bi-ionic conditions, with 4 mM $[Ca^{2+}]_{out}$ and 100 mM $[X^+]_{in}$ (X = Li, Na, K, or Cs), reveal increasing outward current amplitudes from Cs^+ to K^+ to Na^+ to Li^+, reflecting increasing permeability with decreasing ionic radius, consistent with the Eisenman model of permeability through a narrow pore (Eisenman et al., 1967; Eisenman and Horn, 1983). (B) Decreasing permeability for Ca^{2+} over X^+, from Cs^+ to Li^+, is measured by zero-current reversal potentials (E_{Rev}) on IV plots, which represent voltages at which inward-flowing Ca^{2+} and outward-flowing X^+ ions are at equilibrium. (C) Converting E_{Rev} values to relative permeabilities for Ca^{2+} over X^+ (i.e., P_{Ca}/P_X), using the bi-ionic Nernst equation, reveals that TCa$_v$3 is poorly selective for Ca^{2+} over X^+ ions, with a Ca^{2+}-selectivity profile that falls between the extremely Na^+-permeable LCa$_v$3-12a and the moderately Na^+-permeable LCa$_v$3-12b. (D) A zoomed-out view of the IV plot in B reveals three conductance states for TCa$_v$3 (i.e., the slope of current I/I_{max} as a function of depolarizing voltage), with an inward conductance (G_{In}) at voltages that favor inward Ca^{2+} flow, a rectifying conductance across the reversal potential (G_{Rev}) where Ca^{2+} and X^+ ions are competing for permeation, and an outward conductance (G_{Out}) where the voltage favors outward flow of monovalent cations. (E) Comparing the three different conductance states for TCa$_v$3 with those of the two exon 12 variants of LCa$_v$3 and the human Ca$_v$3.1 channel places TCa$_v$3 somewhere between Ca$_v$3.1 and LCa$_v$3-12b. Asterisks depict statistical significance (p-values) for differences between mean conductance relative to TCa$_v$3 (one-way ANOVA; *, $P \leq 0.05$; **, $P \leq 0.005$; ***, $P \leq 0.0005$). All values for B–E represent mean ± SE.

Moroz et al., 2014; Fernandez-Valverde et al., 2015), suggesting that these two phyla lost Ca_v3 channels.

Analysis of various Ca_v3 channel gene exon/intron structures revealed a general trend toward increased intron/exon number from choanoflagellates to vertebrates, with the *Salpingoeca* Ca_v3 gene bearing 13 exons from start codon to stop codon, *Trichoplax* Ca_v3 bearing 28 exons, *Nematostella* Ca_v3a bearing 30 exons, and mouse Cav3.1 bearing 38 exons (Fig. 3). Such an increase in intron number from premetazoans, to early diverging metazoans, to bilaterians is consistent with observed trends at the whole-genome level (King et al., 2008). Interestingly, Ca_v3 channel genes from bilaterians appear to have undergone the most significant changes in intron/exon structure within coding sequences for channel structures associated with modulation of function, such as optional exon 8b found in mouse $Ca_v3.1$ and *Lymnaea* Ca_v3, which regulates channel membrane expression (Senatore and Spafford, 2012); mouse exons 14–17 in the II–III linker, which serve as a hotbed for modulation by kinases and G-proteins (Chemin et al., 2006; Perez-Reyes, 2010b; Senatore et al., 2012); exons 25c and 26 in the III–IV linker, which in both vertebrates and protostome invertebrates cause alterations in channel voltage-gating and kinetics (Senatore and Spafford, 2012); the C terminus, where vertebrate Ca_v3 channels physically interact with other ion channel types such as Ca^{2+}-modulated A-type K^+ channels (Anderson et al., 2010); and SNARE proteins, which facilitate T-type channel involvement in low-threshold exocytosis (Weiss et al., 2012). Indeed, if a similar pattern extends to numerous other gene orthologues in the metazoan genome, it might account for some of the apparent increase in anatomical, cellular, and molecular complexity of vertebrates and bilaterians compared with more early diverging animals (Valentine et al., 1994), in spite of comparable total gene counts.

Despite its comparative simplicity at the gene structure level, the TCa_v3 protein sequence retains all of the hallmark structural features of four-domain channels, with four homologous repeat domains, each containing extracellular turret-containing P-loops separated by pore-forming S5 and S6 helices, and voltage-sensor modules (S1 to S4 helices), with S4 helices packed with positively charged lysine (K) and arginine (R) residues critical for voltage sensing (Fig. 1 A; Catterall, 2010). In addition, TCa_v3 bears the three most prominent structural features that distinguish Ca_v3 channels from Ca_v1 and Ca_v2 types: (1) a selectivity filter motif with two aspartates (D) instead of two glutamates (E) in the P-loops of domains III and IV (i.e., EEDD vs. EEEE); (2) the absence of a calmodulin-binding isoleucine-glutamine (IQ) motif in the C terminus, which permits modulation of Ca_v1 and Ca_v2 channels by cytoplasmic Ca^{2+} influx (Ben-Johny et al., 2014); and (3) a predicted helix-turn-helix gating brake structure in the domain I–II intracellular linker, in an analogous region where Ca_v1 and Ca_v2 channels bind accessory $Ca_v\beta$ subunits via a distinct structure called the α interaction domain (AID; Perez-Reyes, 2010a).The absence of an AID in T-type channels highlights another distinguishing feature, which is a lack of dependence on $Ca_v\beta$ subunits. For Ca_v1 and Ca_v2 channels, $Ca_v\beta$ as well as $Ca_v\alpha_2\delta$ subunits are obligate counterparts that complex with the channels to regulate gating, trafficking, and proteolytic turnover (Arikkath and Campbell, 2003; Richards et al., 2004; Altier et al., 2011). Instead, T-type channels function as separate entities, with an autonomous gating brake serving in lieu of the AID/$Ca_v\beta$ subunit, which nevertheless also regulates channel gating (Perez-Reyes, 2010a). Even the most basal of all known T-type channels, from *S. rosetta*, bears a predicted gating brake motif in its I–II linker (Fig. 2 D). The structural distinction between AIDs of high voltage–activated Ca_v1/Ca_v2 channels and gating brakes of low voltage–activated Ca_v3 channels thus appears to have ancient origins predating Metazoa. However, given the similar helical arrangement that extends into the cytoplasm from the domain I S6 helix, it is conceivable that both structures evolved via divergence from a helical structure present in an ancient Ca_v channel ancestor of Ca_v1/Ca_v2 and Ca_v3 channels.

Localization of TCa_v3 channel in gland cells

In bilaterians, the three types of Ca_v channels are specialized to carry out distinct and pivotal roles in neurons and muscle, and other excitable cell types, where they translate electrical signals of Na_v, K_v, and synaptic ligand-gated cation channels into cellular events by coupling with Ca^{2+}-sensitive cytoplasmic proteins (Berridge, 2006; Rizzuto and Pozzan, 2006). Ca_v1 channels are most classically associated with excitation-contraction coupling in muscle, as well as excitation-transcription coupling in neurons and muscle, and Ca_v2 channels are associated with fast presynaptic exocytosis of neurotransmitters (excitation-secretion coupling; Catterall, 2011). Instead, Ca_v3 channels have long eluded such a stereotyped and ubiquitous classification, where their roles tend to vary depending on cell type, ranging from regulating cellular excitability in select neurons and other excitable cells, to driving low-threshold exocytosis in select neurons and neurosecretory cells, to regulating tone and contraction of various muscle cell types (Perez-Reyes, 2003; Senatore et al., 2012).

Trichoplax is very interesting in its highly simplified cellular body plan, bearing only six cell types: ciliated dorsal and ventral epithelial cells, with ventral epithelial cells responsible for ciliary locomotion (i.e., gliding along hard surfaces); crystal cells, which bear internal birefringent crystals with unknown function (Smith et al., 2014); fiber cells, positioned between the epithelial

cell layers and proposed to be contractile in nature (Behrendt and Ruthmann, 1986; Smith et al., 2014); gland cells, proposed to play roles in paracrine signaling and which resemble neurons and neurosecretory cells in their expression of exocytotic SNARE proteins and membrane-apposed vesicles (Grell and Ruthmann, 1991; Smith et al., 2014); and ventral lipophil cells, also apparently exocytotic in nature but specialized for secretion of hydrolytic enzymes for external digestion of algae during feeding (Smith et al., 2014, 2015). The apparent morphological, anatomical, and ultrastructural similarly of *Trichoplax* cell types with those from more complex animals (i.e., epithelial, neuron/neuroendocrine, muscle, and digestive) is suggestive of cellular homology at the level of genes and proteins. In accordance, the presence of numerous genes in the *Trichoplax* genome crucial for cell-specific functioning (Srivastava et al., 2008), including those for generating and packaging neurotransmitters and neuropeptides (Nikitin, 2015), cellular excitability (e.g., Na_v2 and Kv channels, K^+ leak channels; Senatore et al., 2016), and muscle contraction (Steinmetz et al., 2012), suggests that homologous molecular processes are taking place in some of these cell types.

Here, we extend the apparent homology of gland cells with neurons and neuroendocrine cells in our localization of TCa_v3 to this cell type (Fig. 4), suggesting that the cells undergo rapid fluxes in membrane voltage and transient rises in cytoplasmic [Ca^{2+}], perhaps for engaging Ca^{2+} sensitive elements of the exocytotic machinery. A Ca^{2+} dependence for gland cell exocytosis is further suggested by their expression of complexin, a Ca^{2+}-responsive regulator of the SNARE complex and vesicle fusion (Yoon et al., 2008), and further, by the presence of synaptotagmin in the genome (Srivastava et al., 2008), a key Ca^{2+} sensor for exocytotic release which interacts with complexin during fusion (Tang et al., 2006). We note from our RT-PCR experiment that beyond the Ca_v3 channel, *Trichoplax* expresses Ca_v1 and Ca_v2 channels at the whole-animal mRNA level, as well as the single $Ca_v\beta$ and three $Ca_v\alpha_2\delta$ accessory subunit genes (Fig. 5). If the Ca_v1 and/or Ca_v2 channels are similarly localized to gland cells, TCa_v3 might thus serve to activate the high voltage–activated channels that in turn drive vesicle fusion and exocytosis, as is common in neuroendocrine cells (Mansvelder and Kits, 2000).

Notably, the apparent enrichment of TCa_v3 along the outward-facing area of gland cells (Fig. 4), where the SNARE proteins and membrane-apposed vesicles were previously shown to reside (Smith et al., 2014), is suggestive of a more direct involvement in exocytosis, perhaps driving graded exocytosis before action potential threshold as occurs in select vertebrate and invertebrate neurons and neurosecretory cells (Carbone et al., 2006; Weiss and Zamponi, 2013; Senatore et al., 2016). In vertebrates, a direct interaction between Ca_v3 channels and SNARE proteins syntaxin-1A and SNAP-25 has been documented (Weiss et al., 2012), tethering the channels close to Ca^{2+}-sensitive elements of the exocytotic machinery. The expression of TCa_v3 in gland cells implies that the use of T-type channels in regulating excitation and secretion of neuron/neuroendocrine-like cells might have evolved very early on, at least in the ancestor of placozoans and cnidarians/bilaterians, but perhaps even further back, in the single-celled ancestor of choanoflagellates and metazoans, which possessed a T-type channel gene as well as the core elements of the exocytotic apparatus (King et al., 2008; Fairclough et al., 2013; Moran and Zakon, 2014).

Difficult expression of TCa_v3 in HEK-293T cells

Our first efforts to express the cloned TCa_v3 channel in HEK-293T cells for electrophysiological recording were unsuccessful. Instead, we found that coexpression with rat $Ca_v\beta_1b$ and $Ca_v\alpha_2\delta_1$ accessory subunits of high voltage–activated Ca_v1 and Ca_v2 channels dramatically increased channel expression either as a fusion protein with EGFP, or as a separate protein recordable via whole-cell patch clamp. Interestingly, $Ca_v\beta$ and $Ca_v\alpha_2\delta$ subunits increase membrane expression of high voltage-activated Ca_v channels in part by blocking their internalization and proteasomal degradation (Bernstein and Jones, 2007; Altier et al., 2011; Dolphin, 2012), although the process seems to depend on direct interactions between the subunits and the channel proteins. We do not necessarily expect direct protein–protein interaction between TCa_v3 and the $Ca_v\beta_1b$ and $Ca_v\alpha_2\delta_1$ accessory subunits because such an interaction has yet to be reported for any other cloned vertebrate or invertebrate T-type channel (Dubel et al., 2004; Senatore and Spafford, 2010; Dawson et al., 2014; Cens et al., 2015; Jeong et al., 2015). However, given the overlapping emergence of Ca_v1/Ca_v2 channels, Ca_v3 channels, and the $Ca_v\beta$ subunit in a premetazoan ancestor (Dawson et al., 2014; Moran and Zakon, 2014), the possibility exists that ancestral T-type channels and those from extant basal organisms such as *Trichoplax* physically interact with high voltage-activated $Ca_v\beta_1b$ and $Ca_v\alpha_2\delta_1$ subunits. Here, we found that rat $Ca_v\beta_1b$ and $Ca_v\alpha_2\delta_1$ subunits significantly increased ectopic expression of GFP expressed in the absence of TCa_v3 (Fig. 6), indicating that their effect on ectopic protein expression might at least in part be a result of nonspecific processes.

The biophysical properties of TCa_v3 are consistent with roles in regulating gland cell excitability

One of the most clear cellular functions of Ca_v3 channels is regulating excitability (Perez-Reyes, 2003; Senatore et al., 2012), invoking their low voltages of activation and fast, transient kinetics. For example, mammalian $Ca_v3.2$ calcium channels are enriched in pain-sensing neurons, where they amplify depolarizing sensory in-

puts to increase nociceptive signaling to the spinal cord (Bourinet et al., 2005; Rose et al., 2013). Similarly, in the brain, neuronal Ca_v3 channels are enriched along dendrites (McKay et al., 2006), where they boost postsynaptic excitatory potentials to increase the likelihood of eliciting action potentials (Perez-Reyes, 2003; Senatore et al., 2012). In some cases, the rapid kinetics and low voltages of activation of Ca_v3 channels enable them to function in lieu of Na_v channels where they can drive Ca^{2+} action potentials, as occurs in striated muscle cells from jellyfish (Lin and Spencer, 2001), snail cardiomyocytes (Yeoman et al., 1999; Senatore et al., 2014), and *C. elegans* pharyngeal muscle (Steger et al., 2005).

Here, we show that the biophysical properties of the *Trichoplax* Ca_v3 channel are consistent with a role in regulating excitability in gland cells. Inward Ca^{2+} currents recorded from HEK cells expressing recombinant TCa_v3 emerge upon slight membrane depolarization from a holding potential of −110 mV (Fig. 7, A and B), indicating that like all other in vitro–expressed Ca_v3 channels, TCa_v3 is low voltage activated. In fact, TCa_v3 has the lowest voltage dependency for activation of any cloned T-type channel, with a 5 mV more negative maximal peak inward current than *Lymnaea* Ca_v3, and 10 to 20 mV more negative than the three mammalian isotypes, $Ca_v3.1$ to $Ca_v3.3$ (Fig. 7 B and Table 2). Accordingly, Boltzmann transformation of the peak current–voltage (IV) plot for TCa_v3, into an activation curve (Fig. 7 C), reveals a half-maximal activation considerably left-shifted compared with other Ca_v3 channels. Instead, the channel's half-maximal steady-state inactivation is roughly similar to those of other channels (Table 2). TCa_v3 currents also have reasonably fast activation and inactivation kinetics, which although marginally slower than *Lymnaea* Ca_v3 and the mammalian $Ca_v3.1/Ca_v3.2$ isotypes, are considerably faster than those of $Ca_v3.3$, the slowest of the vertebrate T-type channels (Table 2). TCa_v3 is thus capable of conducting fast inward Ca^{2+} currents upon slight membrane depolarization, with a lower voltage threshold than other T-type channels, while being equally subject to voltage-dependent inactivation. These features indicate that TCa_v3 is poised to be more active at threshold voltages compared with other T-type channels. Furthermore, the particularly slow deactivation kinetics for TCa_v3, at voltages near −70 mV (Table 2), would serve to counter K_v channel–driven action potential repolarization, effectively widening action potentials and increasing net Ca^{2+} influx. Overall, the voltage dependencies and kinetic properties of TCa_v3 are most similar to those of fellow invertebrate T-type, *Lymnaea* Ca_v3, and least to those of mammalian $Ca_v3.3$ (Table 2). What is striking is that upon side-by-side comparison of biophysical properties of various cloned Ca_v3 channels, the structurally divergent *Trichoplax* homologue, which is >600 million years separated from mammalian isotypes, is more similar to mammalian $Ca_v3.1$ and $Ca_v3.2$ than is $Ca_v3.3$. Indeed, there appear to have been strong evolutionary constraints on the TCa_v3 channel to retain a core set of biophysical properties, suggesting that the need for its cellular contributions are conserved even in the absence of neurons and muscle.

An important caveat toward speculation about the physiological roles for TCa_v3 in vivo is that its contributions would ultimately depend on the membrane potential, which is controlled by a milieu of electrogenic proteins. Although *Trichoplax* has the majority of these electrogenic genes (Srivastava et al., 2008; Senatore et al., 2016), suggesting that some of its cells have polarized resting membrane potentials and exhibit rapid fluxes in membrane voltage such as action potentials, the membrane properties of *Trichoplax* cells have yet to be reported. We and others have attempted intracellular recording of isolated *Trichoplax* cells, but their small size (<10-µm diameter) and particular membrane features make obtaining a gigaohm seal during patch-clamp recording particularly difficult. Based on the biophysical properties of TCa_v3, we can speculate that if the resting membrane potential of a typical *Trichoplax* cell sits above −60 mV, the channel would not contribute to excitability because of inactivation (Fig. 7 C). However, transient hyperpolarization from such potentials could recruit the channel by removing inactivation, where it would contribute to postinhibitory rebound (PIR) excitation. In mammals, T-type channel-mediated PIR excitation plays an important role in certain neuronal circuits, such as the thalamus, where postinhibitory Ca^{2+} spikes support rhythmic bursts of action potentials that project to the cortex and gate sensory information during non-REM sleep (Lee et al., 2004; Anderson et al., 2005; Crunelli et al., 2006). Notably, TCa_v3 and the Ca_v3 channel from *Lymnaea* have a slower recovery from inactivation than mammalian channels (Table 2), so they would require more prolonged hyperpolarization to be recruited for PIR excitation. Finally, even if *Trichoplax* cells do not undergo rapid changes in membrane voltage, T-type channels could nevertheless contribute a consistent steam of Ca^{2+} into the cytosol through a window current (Fig. 7 C), which can be used by cells to transition between bimodal resting membrane potentials (Dreyfus et al., 2010) and are associated with cellular proliferation during development and cancer (Lory et al., 2006; Senatore et al., 2012; Gackière et al., 2013).

TCa_v3 resembles mammalian Ca_v3 channels with respect to Na^+ permeation

Previous work examining altered Na^+ permeation of the *Lymnaea* T-type channel, caused by alternative splicing of exons 12a and 12b in a region of the domain II P-loop called the turret, revealed that factors outside of the se-

lectivity filter can nevertheless have important consequences for defining Ca^{2+} versus Na^+ permeation. However, based on these studies, it is difficult to reconcile differences in permeation properties among Ca_v3 channels purely on the structure of exon 12, where in *Lymnaea*, the smaller exon 12a imposes extreme Na^+ permeability (i.e., 93.5% of current carried by Na^+; Fig. 10 B: 1,440 ÷ 1,540% = 93.5%), whereas in mammalian channels, homologous 12a-like exons produce only moderate Na^+ permeability (~21.0%, 24.3%, and 31.3% for $Ca_v3.1$, $Ca_v3.2$, and $Ca_v3.3$, respectively). We found the basal TCa_v3 channel to resemble mammalian channels, with ~29.6% of inward current carried by Na^+, making it statistically indistinguishable from $Ca_v3.2$ and $Ca_v3.3$ (Table 2). Indeed, a low Na^+ permeability for T-type channels bearing exon 12a–like turrets extends to other non-protostome channels that span the lineages between placozoans and mammals, including those from cnidarians (i.e., jellyfish; Lin and Spencer, 2001) and deuterostomes (i.e., echinoderm starfish eggs; Hagiwara et al., 1975), where T-type currents were reported to be carried mostly by Ca^{2+}. Based on the available data, one explanation for the emergence of altered Na^+ permeation in the snail and other protostome T-type channels via exon 12 splicing is that after dupliction of exon 12, structural alterations took place outside of the exon 12 region, rendering 12a-bearing channels more Na^+ permeable. The duplicated exon 12b, unique to protostomes, was possibly adaptated to retain Ca^{2+} conducting channels via enlargement relative to exon 12a by ~11 aa and increase in cysteine content from 0–3 to ~5. In *Lymnaea*, exon 12b produces a channel more in line with non-protostome 12a-like channels, from *Trichoplax* through to mammals, with only ~60.5% of current carried by Na^+.

Interestingly, the degree of co-permeation of Na^+ alongside Ca^{2+} for the various cloned T-type channels seems to hold true even in the presence of Ba^{2+}, which can exhibit increased or decreased permeation relative to Ca^{2+} in a channel-dependent manner. Like rat $Ca_v3.1$, TCa_v3 conducts larger Ca^{2+} currents than Ba^{2+} currents in vitro, whereas rat $Ca_v3.2$, LCa_v3-12a, and LCa_v3-12b all conduct larger Ba^{2+} currents and rat $Ca_v3.3$ conducts equal Ca^{2+} and Ba^{2+} currents (McRory et al., 2001). Despite these differences, the pattern of fold increases in peak inward current for the various channels upon replacement of impermeant external $NMDG^+$ with Na^+ is consistent regardless of whether Ca^{2+} or Ba^{2+} is present in the extracellular solution (Fig. 10). As such, it appears as though the factors that determine macroscopic conduction preference among divalent cations are different from those that determine preference between divalent versus monovalent cations.

Notably, a previous study found that $NMDG^+$ might directly block inward current through T-type channels (Khan et al., 2008), potentially confounding loss of current amplitude caused by replacement of Na^+ in our experiments. However, for the snail T-type channel exon 12a and 12b variants, we previously found that replacement of Na^+ with impermeant $Tris^+$ resulted in a similar pattern of current attenuation compared with $NMDG^+$ (Senatore, 2012), suggesting that the major effect on T-type channel current amplitude in these experiments is caused by Na^+ depletion, and not $NMDG^+$ block.

Ca^{2+} block versus Ca^{2+} over Na^+ selectivity in defining T-type channel cation permeability

We sought to identify different aspects of cation permeation through T-type channels that could account for their varying Na^+ permeabilities. For high voltage–activated Ca_v1 and Ca_v2 channels, which are considerably better than T-types at selecting for Ca^{2+} (e.g., compare 21–90% Na^+ current for Ca_v3 channels with <0.1% for Ca_v1/Ca_v2; Tsien et al., 1987; Sather and McCleskey, 2003; Shcheglovitov et al., 2007; Cheng et al., 2010; Buraei et al., 2014; Tang et al., 2014), selectivity for Ca^{2+} is attributed to the ability of the ion to associate with a high-affinity binding site at the extracellular surface of the pore to repel and block inward Na^+ flux (i.e., Ca^{2+} block). T-type channels are also expected to bind Ca^{2+}, but their reduced selectivity is attributed to a ~10-fold lowered binding affinity and reduced Ca^{2+} block (Shcheglovitov et al., 2007). We compared the Ca^{2+} block properties of various Ca_v3 channels, revealing that TCa_v3 shares with mammalian channels a potent Ca^{2+} block, indicated by rapidly attenuating Na^+ currents as Ca^{2+} is incrementally added to the extracellular solution (Fig. 11). By stark contrast, exon 12 variants of LCa_v3 exhibit a reduction in Ca^{2+} block that is most extreme for LCa_v3-12a, for which the Ca^{2+} titration curve does not exhibit the classic U shape (where decreasing Ca^{2+}-blocked Na^+ currents gradually give way to increasing Ca^{2+} currents as $[Ca^{2+}]_{out}$ increases; Fig. 11 A). Instead, the channels exhibit continued decline through to 10 mM $[Ca^{2+}]_{out}$, reflecting dramatically reduced Ca^{2+} binding affinity in the pore. Altogether, the Ca^{2+} block properties of the different Ca_v3 channels (Fig. 11) correlate with their respective Na^+ permeabilities, apparent in $Na^+/NMDG^+$ replacement experiments (Fig. 10 B): TCa_v3 and human $Ca_v3.1$ have the most potent Ca^{2+} block and lowest Na^+ permeability, and LCa_v3-12a and LCa_v-12b have reduced Ca^{2+} block proportional to their respective increases in Na^+ permeability.

However, we point out a minor inconsistency between our Ca^{2+}-Na^+ permeation data (Fig. 10) and our Ca^{2+} block data (Fig. 11). Whereas the Ca^{2+} block data suggests that at near-physiological external Ca^{2+} concentrations (i.e., 1 mM $[Ca^{2+}]_{out}$), most of the Na^+ current has been blocked for all T-type channels (Fig. 11, A and B), replacement of 135 mM $NMDG^+$ with Na^+ in the presence of 2 mM $[Ca^{2+}]_{out}$ causes significant increases in peak inward current (most marked for

LCa_v3-12a), reflecting additive Na^+ currents over already present Ca^{2+} currents (Fig. 10, A and B). So a question arises: why in 2 mM Ca^{2+} can you observe a considerable additive Na^+ current via $NMDG^+$ replacement, whereas 1–3 mM Ca^{2+} seems to mostly block the Na^+ currents? We explain this inconsistency by noting that in Ca^{2+} block experiments, there are considerable residual currents, ranging in amplitudes from 100–200 pA (i.e., for LCa_v3-12b) to 100–800 pA (for LCa_v3-12a), which persist despite saturation in the Ca^{2+} block effect. We suggest that these residual currents represent combined Ca^{2+}/Na^+ currents, which would be differentially attenuated if the Na^+ ions were to be replaced with impermeant $NMDG^+$, consistent with the Na^+/$NMDG^+$ substitution data (Fig. 10, A, B, E, and F).

TCa_v3 appears to be slightly more Na^+ permeable than human $Ca_v3.1$, in part because of a slightly reduced Ca^{2+}-block and pore Ca^{2+}-binding affinity (Fig. 11, A and B). However, other aspects of the pore might influence the degree of Na^+ permeation. Our bi-ionic reversal potential experiments, which approximate the preference of a given channel pore for inward-flowing Ca^{2+} ions versus outward-flowing monovalents (i.e., Li^+, Na^+, K^+, and Cs^+), revealed that TCa_v3 was considerably less selective for Ca^{2+} than human $Ca_v3.1$ (e.g., P_{Ca}/P_{Na} = 35.61 ± 1.52 vs. 89.56 ± 8.21, respectively), falling between the more Na^+ permeable channels LCa_v3-12a (33.06 ± 1.50) and LCa_v3-12b (41.49 ± 1.98). Indeed, if preference for Ca^{2+} over monovalents measured under bi-ionic conditions was the major determinant for Na^+ permeation, then we would expect TCa_v3 to conduct a much higher proportion of inward Na^+ upon depolarization, most similar to the LCa_v3-12a variant (Fig. 10 B). Instead, the selectivity for Ca^{2+} over monovalents in the TCa_v3 channel pore seems somewhat inconsequential, where 29.6% of the total current is carried by Na^+, which is more similar to $Ca_v3.1$ (21.0%) than either LCa_v3-12b (60.5%) or LCa_v3-12a (93.5%). As such, Ca^{2+} block appears to be more consequential for determining Na^+ permeation than is Ca^{2+} over Na^+ selectivity. Instead, Ca^{2+} selectivity appears to play a more marginal role, possibly accounting for the 8.6% increase in Na^+ permeability for TCa_v3 relative to $Ca_v3.1$.

Finally, we also find an interesting inverse correlation between conductance values across bi-ionic reversal potential (G_{Rev}) and outward monovalent current flow (G_{Out}) versus the potency of the Ca^{2+}-block effect: whereas LCa_v3-12a has the largest G_{Rev} and G_{Out} values and the weakest Ca^{2+} block, $Ca_v3.1$ has the smallest G_{Rev} and G_{Out} values and the strongest Ca^{2+} block (compare Fig. 11 B with the top two panels of Fig. 12 E). This is not surprising because G_{Rev} and G_{Out} should reflect the pore's permeability to outward-flowing monovalents, against external Ca^{2+} which seeks to bind the extracellular high-affinity site. However, there is a slight inconsistency in this correlation, where G_{Rev} and G_{Out} conductance values for TCa_v3 are significantly larger than $Ca_v3.1$, despite both channels bearing similarly potent Ca^{2+} block properties. Instead, the conductance values for TCa_v3 lie between those of $Ca_v3.1$ and the two exon 12 splice variants of LCa_v3. Thus, conductance across the reversal potential and during outward current flow though T-type channels might depend on a combination of both affinity for Ca^{2+} at the external pore surface (where TCa_v3 and $Ca_v3.1$ are similar), and pore Ca^{2+} versus Na^+ permeability (where TCa_v3 and LCa_v3 are more similar).

In conclusion, we find evidence that for T-type channels, Ca^{2+} block—and not Ca^{2+} versus Na^+ selectivity—best correlates with the degree of inward Na^+ permeation under simulated physiological conditions. For *Trichoplax*, which lives in seawater, the abundance of external Ca^{2+} must ensure efficient saturation of the Ca^{2+} block effect, rendering the channels mostly permeable to Ca^{2+}. Here, our studies were performed using salines that are compatible with HEK-293T cells, with reduced ionic concentrations and osmolarity across both sides of the membrane compared with seawater. In future studies, it will be interesting to evaluate the consequences of altered ion concentrations on TCa_v3 biophysical, permeation, and pharmacological properties (and indeed other ion channel types), where evolutionary transitions from seawater to land/freshwater environments, and perhaps back again, would likely require some level of adaptation in channel function, such that contributions to cellular excitability and Ca^{2+} influx remain within acceptable parameters.

ACKNOWLEDGMENTS

We thank Drs. David Spafford and Paul S. Katz for providing support to A. Senatore during the preliminary stages of this research, Dr. Arnaud Monteil for preliminary Western blotting of the TCa_v3 channel protein, Farid R. Ahmadli for help analyzing Ca_v3 channel gene sequences, and Dr. Andreas Heyland for providing the *Trichoplax* specimens used for sequencing and cloning of the TCa_v3 channel cDNA.

This work was funded by a National Science and Engineering Research Council of Canada (NSERC) Discovery Grant (RGPIN-2016-06023), a Canadian Foundation for Innovation Grant (CFI Project 35297), University of Toronto Mississauga start-up funds, and an NSERC postdoctoral fellowship (PDF-43851-2013) to A. Senatore.

The authors declare no competing financial interests.

Richard W. Aldrich served as editor.

Submitted: 28 August 2016
Accepted: 7 February 2017

REFERENCES

Altier, C., A. Garcia-Caballero, B. Simms, H. You, L. Chen, J. Walcher, H.W. Tedford, T. Hermosilla, and G.W. Zamponi. 2011. The Cavβ subunit prevents RFP2-mediated ubiquitination and proteasomal degradation of L-type channels. *Nat. Neurosci.* 14:173–180. http://dx.doi.org/10.1038/nn.2712

Anderson, D., W.H. Mehaffey, M. Iftinca, R. Rehak, J.D. Engbers, S. Hameed, G.W. Zamponi, and R.W. Turner. 2010. Regulation of

neuronal activity by Ca_v3-K_v4 channel signaling complexes. *Nat. Neurosci.* 13:333–337. http://dx.doi.org/10.1038/nn.2493

Anderson, M.P., T. Mochizuki, J. Xie, W. Fischler, J.P. Manger, E.M. Talley, T.E. Scammell, and S. Tonegawa. 2005. Thalamic $Ca_v3.1$ T-type Ca^{2+} channel plays a crucial role in stabilizing sleep. *Proc. Natl. Acad. Sci. USA.* 102:1743–1748. http://dx.doi.org/10.1073/pnas.0409644102

Arias-Olguín, I.I., I. Vitko, M. Fortuna, J.P. Baumgart, S. Sokolova, I.A. Shumilin, A. Van Deusen, M. Soriano-García, J.C. Gomora, and E. Perez-Reyes. 2008. Characterization of the gating brake in the I-II loop of $Ca_v3.2$ T-type Ca^{2+} channels. *J. Biol. Chem.* 283:8136–8144. http://dx.doi.org/10.1074/jbc.M708761200

Arikkath, J., and K.P. Campbell. 2003. Auxiliary subunits: Essential components of the voltage-gated calcium channel complex. *Curr. Opin. Neurobiol.* 13:298–307. http://dx.doi.org/10.1016/S0959-4388(03)00066-7

Behrendt, G., and A. Ruthmann. 1986. The cytoskeleton of the fiber cells of *Trichoplax adhaerens* (Placozoa). *Zoomorphology.* 106:123–130. http://dx.doi.org/10.1007/BF00312114

Ben-Johny, M., P.S. Yang, J. Niu, W. Yang, R. Joshi-Mukherjee, and D.T. Yue. 2014. Conservation of Ca^{2+}/calmodulin regulation across Na and Ca^{2+} channels. *Cell.* 157:1657–1670. http://dx.doi.org/10.1016/j.cell.2014.04.035

Bernstein, G.M., and O.T. Jones. 2007. Kinetics of internalization and degradation of N-type voltage-gated calcium channels: Role of the α_2/δ subunit. *Cell Calcium.* 41:27–40. http://dx.doi.org/10.1016/j.ceca.2006.04.010

Berridge, M.J. 2006. Calcium microdomains: Organization and function. *Cell Calcium.* 40:405–412. http://dx.doi.org/10.1016/j.ceca.2006.09.002

Bourinet, E., A. Alloui, A. Monteil, C. Barrère, B. Couette, O. Poirot, A. Pages, J. McRory, T.P. Snutch, A. Eschalier, and J. Nargeot. 2005. Silencing of the $Ca_v3.2$ T-type calcium channel gene in sensory neurons demonstrates its major role in nociception. *EMBO J.* 24:315–324. http://dx.doi.org/10.1038/sj.emboj.7600515

Buraei, Z., H. Liang, and K.S. Elmslie. 2014. Voltage control of Ca^{2+} permeation through N-type calcium ($Ca_V2.2$) channels. *J. Gen. Physiol.* 144:207–220. http://dx.doi.org/10.1085/jgp.201411201

Cain, S.M., and T.P. Snutch. 2010. Contributions of T-type calcium channel isoforms to neuronal firing. *Channels (Austin).* 4:475–482. http://dx.doi.org/10.4161/chan.4.6.14106

Capella-Gutiérrez, S., J.M. Silla-Martínez, and T. Gabaldón. 2009. trimAl: A tool for automated alignment trimming in large-scale phylogenetic analyses. *Bioinformatics.* 25:1972–1973. http://dx.doi.org/10.1093/bioinformatics/btp348

Carbone, E., A. Giancippoli, A. Marcantoni, D. Guido, and V. Carabelli. 2006. A new role for T-type channels in fast "low-threshold" exocytosis. *Cell Calcium.* 40:147–154. http://dx.doi.org/10.1016/j.ceca.2006.04.019

Catterall, W.A. 2010. Ion channel voltage sensors: Structure, function, and pathophysiology. *Neuron.* 67:915–928. http://dx.doi.org/10.1016/j.neuron.2010.08.021

Catterall, W.A. 2011. Voltage-gated calcium channels. *Cold Spring Harb. Perspect. Biol.* 3:a003947. http://dx.doi.org/10.1101/cshperspect.a003947

Cens, T., M. Rousset, C. Collet, M. Charreton, L. Garnery, Y. Le Conte, M. Chahine, J.-C. Sandoz, and P. Charnet. 2015. Molecular characterization and functional expression of the *Apis mellifera* voltage-dependent Ca^{2+} channels. *Insect Biochem. Mol. Biol.* 58:12–27. http://dx.doi.org/10.1016/j.ibmb.2015.01.005

Chemin, J., A. Monteil, E. Bourinet, J. Nargeot, and P. Lory. 2001. Alternatively spliced α(1G) ($Ca_V3.1$) intracellular loops promote specific T-type Ca^{2+} channel gating properties. *Biophys. J.* 80:1238–1250. http://dx.doi.org/10.1016/S0006-3495(01)76100-0

Chemin, J., A. Monteil, E. Perez-Reyes, E. Bourinet, J. Nargeot, and P. Lory. 2002. Specific contribution of human T-type calcium channel isotypes (α_{1G}, α_{1H} and α_{1I}) to neuronal excitability. *J. Physiol.* 540:3–14. http://dx.doi.org/10.1113/jphysiol.2001.013269

Chemin, J., A. Traboulsie, and P. Lory. 2006. Molecular pathways underlying the modulation of T-type calcium channels by neurotransmitters and hormones. *Cell Calcium.* 40:121–134. http://dx.doi.org/10.1016/j.ceca.2006.04.015

Cheng, R.C., D.B. Tikhonov, and B.S. Zhorov. 2010. Structural modeling of calcium binding in the selectivity filter of the L-type calcium channel. *Eur. Biophys. J.* 39:839–853. http://dx.doi.org/10.1007/s00249-009-0574-2

Clapham, D.E. 2007. Calcium signaling. *Cell.* 131:1047–1058. http://dx.doi.org/10.1016/j.cell.2007.11.028

Clarke, T.F. IV, and P.L. Clark. 2008. Rare codons cluster. *PLoS One.* 3:e3412. http://dx.doi.org/10.1371/journal.pone.0003412

Crunelli, V., D.W. Cope, and S.W. Hughes. 2006. Thalamic T-type Ca^{2+} channels and NREM sleep. *Cell Calcium.* 40:175–190. http://dx.doi.org/10.1016/j.ceca.2006.04.022

Dawson, T.F., A.N. Boone, A. Senatore, J. Piticaru, S. Thiyagalingam, D. Jackson, A. Davison, and J.D. Spafford. 2014. Gene splicing of an invertebrate beta subunit ($LCa_v\beta$) in the N-terminal and HOOK domains and its regulation of LCa_v1 and LCa_v2 calcium channels. *PLoS One.* 9:e92941. http://dx.doi.org/10.1371/journal.pone.0092941

Dolphin, A.C. 2012. Calcium channel auxiliary $\alpha_2\delta$ and β subunits: trafficking and one step beyond. *Nat. Rev. Neurosci.* 13:542–555 (published erratum appears in *Nat. Rev. Neurosci.* 2012. 13:664). http://dx.doi.org/10.1038/nrn3317

Dreyfus, F.M., A. Tscherter, A.C. Errington, J.J. Renger, H.S. Shin, V.N. Uebele, V. Crunelli, R.C. Lambert, and N. Leresche. 2010. Selective T-type calcium channel block in thalamic neurons reveals channel redundancy and physiological impact of I(T) window. *J. Neurosci.* 30:99–109. http://dx.doi.org/10.1523/JNEUROSCI.4305-09.2010

Dubel, S.J., C. Altier, S. Chaumont, P. Lory, E. Bourinet, and J. Nargeot. 2004. Plasma membrane expression of T-type calcium channel α_1 subunits is modulated by high voltage-activated auxiliary subunits. *J. Biol. Chem.* 279:29263–29269. http://dx.doi.org/10.1074/jbc.M313450200

Edgar, R.C. 2004. MUSCLE: Multiple sequence alignment with high accuracy and high throughput. *Nucleic Acids Res.* 32:1792–1797. http://dx.doi.org/10.1093/nar/gkh340

Eisenman, G., and R. Horn. 1983. Ionic selectivity revisited: The role of kinetic and equilibrium processes in ion permeation through channels. *J. Membr. Biol.* 76:197–225. http://dx.doi.org/10.1007/BF01870364

Eisenman, G., J.P. Sandblom, and J.L. Walker Jr. 1967. Membrane structure and ion permeation. Study of ion exchange membrane structure and function is relevant to analysis of biological ion permeation. *Science.* 155:965–974. http://dx.doi.org/10.1126/science.155.3765.965

Emerick, M.C., R. Stein, R. Kunze, M.M. McNulty, M.R. Regan, D.A. Hanck, and W.S. Agnew. 2006. Profiling the array of $Ca_v3.1$ variants from the human T-type calcium channel gene CACNA1G: alternative structures, developmental expression, and biophysical variations. *Proteins.* 64:320–342. http://dx.doi.org/10.1002/prot.20877

Fairclough, S.R., Z. Chen, E. Kramer, Q. Zeng, S. Young, H.M. Robertson, E. Begovic, D.J. Richter, C. Russ, M.J. Westbrook, et al. 2013. Premetazoan genome evolution and the regulation of cell differentiation in the choanoflagellate *Salpingoeca rosetta*. *Genome Biol.* 14:R15. http://dx.doi.org/10.1186/gb-2013-14-2-r15

Fernandez-Valverde, S.L., A.D. Calcino, and B.M. Degnan. 2015. Deep developmental transcriptome sequencing uncovers

numerous new genes and enhances gene annotation in the sponge *Amphimedon queenslandica*. *BMC Genomics*. 16:387. http://dx.doi.org/10.1186/s12864-015-1588-z

Francis, W.R., N.C. Shaner, L.M. Christianson, M.L. Powers, and S.H. Haddock. 2015. Occurrence of isopenicillin-N-synthase homologs in bioluminescent ctenophores and implications for coelenterazine biosynthesis. *PLoS One*. 10:e0128742. http://dx.doi.org/10.1371/journal.pone.0128742

Fredman, D., M. Schwaiger, F. Rentzsch, and U. Technau. 2013. *Nematostella vectensis* transcriptome and gene models v2.0. Available at https://figshare.com/articles/Nematostella_vectensis_transcriptome_and_gene_models_v2_0/807696.

Gackière, F., M. Warnier, M. Katsogiannou, S. Derouiche, P. Delcourt, E. Dewailly, C. Slomianny, S. Humez, N. Prevarskaya, M. Roudbaraki, and P. Mariot. 2013. Functional coupling between large-conductance potassium channels and $Ca_v3.2$ voltage-dependent calcium channels participates in prostate cancer cell growth. *Biol. Open*. 2:941–951. http://dx.doi.org/10.1242/bio.20135215

Gerstein, M.B., Z.J. Lu, E.L. Van Nostrand, C. Cheng, B.I. Arshinoff, T. Liu, K.Y. Yip, R. Robilotto, A. Rechtsteiner, K. Ikegami, et al. modENCODE Consortium. 2010. Integrative analysis of the *Caenorhabditis elegans* genome by the modENCODE project. *Science*. 330:1775–1787. http://dx.doi.org/10.1126/science.1196914

Gomora, J.C., J. Murbartián, J.M. Arias, J.H. Lee, and E. Perez-Reyes. 2002. Cloning and expression of the human T-type channel $Ca_v3.3$: insights into prepulse facilitation. *Biophys. J.* 83:229–241. http://dx.doi.org/10.1016/S0006-3495(02)75164-3

Graveley, B.R., A.N. Brooks, J.W. Carlson, M.O. Duff, J.M. Landolin, L. Yang, C.G. Artieri, M.J. van Baren, N. Boley, B.W. Booth, et al. 2011. The developmental transcriptome of *Drosophila melanogaster*. *Nature*. 471:473–479. http://dx.doi.org/10.1038/nature09715

Grell, K.G., and A. Ruthmann. 1991. Placozoa. *In* Microscopic Anatomy of Invertebrates. Volume 2: Placozoa, Porifera, Cnidaria, and Ctenophora. F.W. Harrison and J.A. Westfall, editors. Wiley-Liss, Inc., Hoboken, NJ. 13–27.

Gustafsson, C., S. Govindarajan, and J. Minshull. 2004. Codon bias and heterologous protein expression. *Trends Biotechnol.* 22:346–353. http://dx.doi.org/10.1016/j.tibtech.2004.04.006

Hagiwara, S., S. Ozawa, and O. Sand. 1975. Voltage clamp analysis of two inward current mechanisms in the egg cell membrane of a starfish. *J. Gen. Physiol.* 65:617–644. http://dx.doi.org/10.1085/jgp.65.5.617

Heyland, A., R. Croll, S. Goodall, J. Kranyak, and R. Wyeth. 2014. *Trichoplax adhaerens*, an enigmatic basal metazoan with potential. *In* Developmental Biology of the Sea Urchin and Other Marine Invertebrates: Methods and Protocols. D.J. Carroll, and S.A. Stricker, editors. Humana Press, New York. 45–61. http://dx.doi.org/10.1007/978-1-62703-974-1_4

Hille, B. 2001. Ion channels of excitable membranes. Third edition. Sinauer, Sunderland, MA. 814 pp.

Huff, J. 2015. The Airyscan detector from ZEISS: Confocal imaging with improved signal-to-noise ratio and super-resolution. *Nat. Methods*. 12. Available at: http://www.nature.com/nmeth/journal/v12/n12/full/nmeth.f.388.html

Jeong, K., S. Lee, H. Seo, Y. Oh, D. Jang, J. Choe, D. Kim, J.-H. Lee, and W.D. Jones. 2015. Ca-α1T, a fly T-type Ca^{2+} channel, negatively modulates sleep. *Sci. Rep.* 5:17893. http://dx.doi.org/10.1038/srep17893

Kang, H.W., J.Y. Park, S.W. Jeong, J.A. Kim, H.J. Moon, E. Perez-Reyes, and J.H. Lee. 2006. A molecular determinant of nickel inhibition in $Ca_v3.2$ T-type calcium channels. *J. Biol. Chem.* 281:4823–4830. http://dx.doi.org/10.1074/jbc.M510197200

Kang, H.W., I. Vitko, S.S. Lee, E. Perez-Reyes, and J.H. Lee. 2010. Structural determinants of the high affinity extracellular zinc binding site on $Ca_v3.2$ T-type calcium channels. *J. Biol. Chem.* 285:3271–3281. http://dx.doi.org/10.1074/jbc.M109.067660

Khan, N., I.P. Gray, C.A. Obejero-Paz, and S.W. Jones. 2008. Permeation and gating in $Ca_V3.1$ (α_{1G}) T-type calcium channels effects of Ca^{2+}, Ba^{2+}, Mg^{2+}, and Na^{+}. *J. Gen. Physiol.* 132:223–238. http://dx.doi.org/10.1085/jgp.200809986

King, N., M.J. Westbrook, S.L. Young, A. Kuo, M. Abedin, J. Chapman, S. Fairclough, U. Hellsten, Y. Isogai, I. Letunic, et al. 2008. The genome of the choanoflagellate *Monosiga brevicollis* and the origin of metazoans. *Nature*. 451:783–788. http://dx.doi.org/10.1038/nature06617

Kobayashi, H. 2015. Inducible suppression of global translation by overuse of rare codons. *Appl. Environ. Microbiol.* 81:2544–2553. http://dx.doi.org/10.1128/AEM.03708-14

Kozak, M. 1986. Point mutations define a sequence flanking the AUG initiator codon that modulates translation by eukaryotic ribosomes. *Cell*. 44:283–292. http://dx.doi.org/10.1016/0092-8674(86)90762-2

Kumar, S., G. Stecher, and K. Tamura. 2016. MEGA7: Molecular Evolutionary Genetics Analysis version 7.0 for bigger datasets. *Mol. Biol. Evol.* 33:1870–1874. http://dx.doi.org/10.1093/molbev/msw054

Lee, J., D. Kim, and H.-S. Shin. 2004. Lack of delta waves and sleep disturbances during non-rapid eye movement sleep in mice lacking $\alpha 1_G$-subunit of T-type calcium channels. *Proc. Natl. Acad. Sci. USA*. 101:18195–18199. http://dx.doi.org/10.1073/pnas.0408089101

Lin, Y.C., and A.N. Spencer. 2001. Calcium currents from jellyfish striated muscle cells: Preservation of phenotype, characterisation of currents and channel localisation. *J. Exp. Biol.* 204:3717–3726.

Lory, P., I. Bidaud, and J. Chemin. 2006. T-type calcium channels in differentiation and proliferation. *Cell Calcium*. 40:135–146. http://dx.doi.org/10.1016/j.ceca.2006.04.017

Mansvelder, H.D., and K.S. Kits. 2000. Calcium channels and the release of large dense core vesicles from neuroendocrine cells: Spatial organization and functional coupling. *Prog. Neurobiol.* 62:427–441. http://dx.doi.org/10.1016/S0301-0082(00)00003-4

McGuffin, L.J., K. Bryson, and D.T. Jones. 2000. The PSIPRED protein structure prediction server. *Bioinformatics*. 16:404–405. http://dx.doi.org/10.1093/bioinformatics/16.4.404

McKay, B.E., J.E. McRory, M.L. Molineux, J. Hamid, T.P. Snutch, G.W. Zamponi, and R.W. Turner. 2006. Ca_V3 T-type calcium channel isoforms differentially distribute to somatic and dendritic compartments in rat central neurons. *Eur. J. Neurosci.* 24:2581–2594. http://dx.doi.org/10.1111/j.1460-9568.2006.05136.x

McRory, J.E., C.M. Santi, K.S. Hamming, J. Mezeyova, K.G. Sutton, D.L. Baillie, A. Stea, and T.P. Snutch. 2001. Molecular and functional characterization of a family of rat brain T-type calcium channels. *J. Biol. Chem.* 276:3999–4011. http://dx.doi.org/10.1074/jbc.M008215200

Moran, Y., and H.H. Zakon. 2014. The evolution of the four subunits of voltage-gated calcium channels: Ancient roots, increasing complexity, and multiple losses. *Genome Biol. Evol.* 6:2210–2217. http://dx.doi.org/10.1093/gbe/evu177

Moran, Y., M.G. Barzilai, B.J. Liebeskind, and H.H. Zakon. 2015. Evolution of voltage-gated ion channels at the emergence of metazoa. *J. Exp. Biol.* 218:515–525. http://dx.doi.org/10.1242/jeb.110270

Moroz, L.L., and A.B. Kohn. 2015. Unbiased view of synaptic and neuronal gene complement in ctenophores: Are there pan-neuronal and pan-synaptic genes across metazoa? *Integr. Comp. Biol.* 55:1028–1049.

Moroz, L.L., K.M. Kocot, M.R. Citarella, S. Dosung, T.P. Norekian, I.S. Povolotskaya, A.P. Grigorenko, C. Dailey, E. Berezikov, K.M. Buckley, et al. 2014. The ctenophore genome and the evolutionary origins of neural systems. *Nature.* 510:109–114. http://dx.doi.org/10.1038/nature13400

Morris, S.C. 1998. Early metazoan evolution: Reconciling paleontology and molecular biology. *Am. Zool.* 38:867–877. http://dx.doi.org/10.1093/icb/38.6.867

Nikitin, M. 2015. Bioinformatic prediction of *Trichoplax adhaerens* regulatory peptides. *Gen. Comp. Endocrinol.* 212:145–155. http://dx.doi.org/10.1016/j.ygcen.2014.03.049

Obejero-Paz, C.A., I.P. Gray, and S.W. Jones. 2008. Ni^{2+} block of $Ca_V3.1$ (α1G) T-type calcium channels. *J. Gen. Physiol.* 132:239–250. http://dx.doi.org/10.1085/jgp.200809988

Ohkubo, T., Y. Inoue, T. Kawarabayashi, and K. Kitamura. 2005. Identification and electrophysiological characteristics of isoforms of T-type calcium channel $Ca_v3.2$ expressed in pregnant human uterus. *Cell. Physiol. Biochem.* 16:245–254. http://dx.doi.org/10.1159/000089850

Pan, Q., O. Shai, L.J. Lee, B.J. Frey, and B.J. Blencowe. 2008. Deep surveying of alternative splicing complexity in the human transcriptome by high-throughput sequencing. *Nat. Genet.* 40:1413–1415. http://dx.doi.org/10.1038/ng.259

Perez-Reyes, E. 2003. Molecular physiology of low-voltage-activated t-type calcium channels. *Physiol. Rev.* 83:117–161. http://dx.doi.org/10.1152/physrev.00018.2002

Perez-Reyes, E. 2010a. Characterization of the gating brake in the I-II loop of Ca_V3 T-type calcium channels. *Channels (Austin).* 4:453–458. http://dx.doi.org/10.4161/chan.4.6.12889

Perez-Reyes, E. 2010b. G protein-mediated inhibition of $Ca_v3.2$ T-type channels revisited. *Mol. Pharmacol.* 77:136–138. http://dx.doi.org/10.1124/mol.109.062133

Pisani, D., W. Pett, M. Dohrmann, R. Feuda, O. Rota-Stabelli, H. Philippe, N. Lartillot, and G. Wörheide. 2015. Genomic data do not support comb jellies as the sister group to all other animals. *Proc. Natl. Acad. Sci. USA.* 112:15402–15407. http://dx.doi.org/10.1073/pnas.1518127112

Presnyak, V., N. Alhusaini, Y.-H. Chen, S. Martin, N. Morris, N. Kline, S. Olson, D. Weinberg, K.E. Baker, B.R. Graveley, and J. Coller. 2015. Codon optimality is a major determinant of mRNA stability. *Cell.* 160:1111–1124. http://dx.doi.org/10.1016/j.cell.2015.02.029

Ramani, A.K., J.A. Calarco, Q. Pan, S. Mavandadi, Y. Wang, A.C. Nelson, L.J. Lee, Q. Morris, B.J. Blencowe, M. Zhen, and A.G. Fraser. 2011. Genome-wide analysis of alternative splicing in *Caenorhabditis elegans*. *Genome Res.* 21:342–348. http://dx.doi.org/10.1101/gr.114645.110

Richards, M.W., A.J. Butcher, and A.C. Dolphin. 2004. Ca^{2+} channel β-subunits: Structural insights AID our understanding. *Trends Pharmacol. Sci.* 25:626–632. http://dx.doi.org/10.1016/j.tips.2004.10.008

Rizzuto, R., and T. Pozzan. 2006. Microdomains of intracellular Ca^{2+}: Molecular determinants and functional consequences. *Physiol. Rev.* 86:369–408. http://dx.doi.org/10.1152/physrev.00004.2005

Rose, K.E., N. Lunardi, A. Boscolo, X. Dong, A. Erisir, V. Jevtovic-Todorovic, and S.M. Todorovic. 2013. Immunohistological demonstration of $Ca_V3.2$ T-type voltage-gated calcium channel expression in soma of dorsal root ganglion neurons and peripheral axons of rat and mouse. *Neuroscience.* 250:263–274. http://dx.doi.org/10.1016/j.neuroscience.2013.07.005

Ryan, J.F., K. Pang, C.E. Schnitzler, A.-D. Nguyen, R.T. Moreland, D.K. Simmons, B.J. Koch, W.R. Francis, P. Havlak, S.A. Smith, et al. NISC Comparative Sequencing Program. 2013. The genome of the ctenophore *Mnemiopsis leidyi* and its implications for cell type evolution. *Science.* 342:1242592. http://dx.doi.org/10.1126/science.1242592

Sather, W.A., and E.W. McCleskey. 2003. Permeation and selectivity in calcium channels. *Annu. Rev. Physiol.* 65:133–159. http://dx.doi.org/10.1146/annurev.physiol.65.092101.142345

Schierwater, B. 2005. My favorite animal, *Trichoplax adhaerens*. *BioEssays.* 27:1294–1302. http://dx.doi.org/10.1002/bies.20320

Schneider, C.A., W.S. Rasband, and K.W. Eliceiri. 2012. NIH Image to ImageJ: 25 years of image analysis. *Nat. Methods.* 9:671–675. http://dx.doi.org/10.1038/nmeth.2089

Senatore, A. 2012. Alternative splicing of *Lymnaea* Ca_v3 and NALCN ion channel genes serves to alter biophysical properties, membrane expression, and ion selectivity. UWSpace. Available at https://uwspace.uwaterloo.ca/handle/10012/6926

Senatore, A., and J.D. Spafford. 2010. Transient and big are key features of an invertebrate T-type channel (LCa_v3) from the central nervous system of *Lymnaea stagnalis*. *J. Biol. Chem.* 285:7447–7458. http://dx.doi.org/10.1074/jbc.M109.090753

Senatore, A., and J.D. Spafford. 2012. Gene transcription and splicing of T-type channels are evolutionarily-conserved strategies for regulating channel expression and gating. *PLoS One.* 7:e37409 (published erratum appears in *PLoS One*. 2013. 8. https://doi.org/10.1371/annotation/9d69fd63-4378-4e05-b2ad-2a5c98561223). http://dx.doi.org/10.1371/journal.pone.0037409

Senatore, A., A.N. Boone, and J.D. Spafford. 2011. Optimized transfection strategy for expression and electrophysiological recording of recombinant voltage-gated ion channels in HEK-293T cells. *J. Vis. Exp.* (47):2314.

Senatore, A., B.S. Zhorov, and J.D. Spafford. 2012. Ca_V3 T-type calcium channels. *WIREs Membrane Transport and Signaling.* 1:467–491. http://dx.doi.org/10.1002/wmts.41

Senatore, A., W. Guan, A.N. Boone, and J.D. Spafford. 2014. T-type channels become highly permeable to sodium ions using an alternative extracellular turret region (S5-P) outside the selectivity filter. *J. Biol. Chem.* 289:11952–11969. http://dx.doi.org/10.1074/jbc.M114.551473

Senatore, A., H. Raiss, and P. Le. 2016. Physiology and evolution of voltage-gated calcium channels in early diverging animal phyla: Cnidaria, placozoa, porifera and ctenophora. *Front. Physiol.* 7:481. http://dx.doi.org/10.3389/fphys.2016.00481

Sharp, P.M., and W.-H. Li. 1987. The codon Adaptation Index–a measure of directional synonymous codon usage bias, and its potential applications. *Nucleic Acids Res.* 15:1281–1295. http://dx.doi.org/10.1093/nar/15.3.1281

Shcheglovitov, A., P. Kostyuk, and Y. Shuba. 2007. Selectivity signatures of three isoforms of recombinant T-type Ca^{2+} channels. *Biochim. Biophys. Acta.* 1768:1406–1419. http://dx.doi.org/10.1016/j.bbamem.2007.02.017

Shcheglovitov, A., I. Vitko, I. Bidaud, J.P. Baumgart, M.F. Navarro-Gonzalez, T.H. Grayson, P. Lory, C.E. Hill, and E. Perez-Reyes. 2008. Alternative splicing within the I-II loop controls surface expression of T-type $Ca_v3.1$ calcium channels. *FEBS Lett.* 582:3765–3770. http://dx.doi.org/10.1016/j.febslet.2008.10.013

Smith, C.L., F. Varoqueaux, M. Kittelmann, R.N. Azzam, B. Cooper, C.A. Winters, M. Eitel, D. Fasshauer, and T.S. Reese. 2014. Novel cell types, neurosecretory cells, and body plan of the early-diverging metazoan *Trichoplax adhaerens*. *Curr. Biol.* 24:1565–1572. http://dx.doi.org/10.1016/j.cub.2014.05.046

Smith, C.L., N. Pivovarova, and T.S. Reese. 2015. Coordinated feeding behavior in *Trichoplax*, an animal without snapses. *PLoS One.* 10:e0136098. http://dx.doi.org/10.1371/journal.pone.0136098

Spafford, J.D., A.N. Spencer, and W.J. Gallin. 1999. Genomic organization of a voltage-gated Na^+ channel in a hydrozoan jellyfish: Insights into the evolution of voltage-gated Na^+ channel genes. *Receptors Channels.* 6:493–506.

Srivastava, M., E. Begovic, J. Chapman, N.H. Putnam, U. Hellsten, T. Kawashima, A. Kuo, T. Mitros, A. Salamov, M.L. Carpenter, et

al. 2008. The *Trichoplax* genome and the nature of placozoans. *Nature*. 454:955–960. http://dx.doi.org/10.1038/nature07191

Srivastava, M., O. Simakov, J. Chapman, B. Fahey, M.E.A. Gauthier, T. Mitros, G.S. Richards, C. Conaco, M. Dacre, U. Hellsten, et al. 2010. The *Amphimedon queenslandica* genome and the evolution of animal complexity. *Nature*. 466:720–726. http://dx.doi.org/10.1038/nature09201

Steger, K.A., B.B. Shtonda, C. Thacker, T.P. Snutch, and L. Avery. 2005. The *C. elegans* T-type calcium channel CCA-1 boosts neuromuscular transmission. *J. Exp. Biol.* 208:2191–2203. http://dx.doi.org/10.1242/jeb.01616

Steinmetz, P.R., J.E. Kraus, C. Larroux, J.U. Hammel, A. Amon-Hassenzahl, E. Houliston, G. Wörheide, M. Nickel, B.M. Degnan, and U. Technau. 2012. Independent evolution of striated muscles in cnidarians and bilaterians. *Nature*. 487:231–234. http://dx.doi.org/10.1038/nature11180

Stephens, R.F., W. Guan, B.S. Zhorov, and J.D. Spafford. 2015. Selectivity filters and cysteine-rich extracellular loops in voltage-gated sodium, calcium, and NALCN channels. *Front. Physiol.* 6:153. http://dx.doi.org/10.3389/fphys.2015.00153

Syed, T., and B. Schierwater. 2002. The evolution of the Placozoa: a new morphological model. *Senckenbergiana lethaea*. 82:315–324. http://dx.doi.org/10.1007/BF03043791

Talavera, K., and B. Nilius. 2006. Biophysics and structure-function relationship of T-type Ca^{2+} channels. *Cell Calcium*. 40:97–114. http://dx.doi.org/10.1016/j.ceca.2006.04.013

Tang, J., A. Maximov, O.-H. Shin, H. Dai, J. Rizo, and T.C. Südhof. 2006. A complexin/synaptotagmin 1 switch controls fast synaptic vesicle exocytosis. *Cell*. 126:1175–1187. http://dx.doi.org/10.1016/j.cell.2006.08.030

Tang, L., T.M. Gamal El-Din, J. Payandeh, G.Q. Martinez, T.M. Heard, T. Scheuer, N. Zheng, and W.A. Catterall. 2014. Structural basis for Ca^{2+} selectivity of a voltage-gated calcium channel. *Nature*. 505:56–61. http://dx.doi.org/10.1038/nature12775

Taylor, J.T., X.B. Zeng, J.E. Pottle, K. Lee, A.R. Wang, S.G. Yi, J.A. Scruggs, S.S. Sikka, and M. Li. 2008. Calcium signaling and T-type calcium channels in cancer cell cycling. *World J. Gastroenterol.* 14:4984–4991. http://dx.doi.org/10.3748/wjg.14.4984

Tomlinson, W.J., A. Stea, E. Bourinet, P. Charnet, J. Nargeot, and T.P. Snutch. 1993. Functional properties of a neuronal class C L-type calcium channel. *Neuropharmacology*. 32:1117–1126. http://dx.doi.org/10.1016/0028-3908(93)90006-O

Tsien, R.W., P. Hess, E.W. McCleskey, and R.L. Rosenberg. 1987. Calcium channels: Mechanisms of selectivity, permeation, and block. *Annu. Rev. Biophys. Biophys. Chem.* 16:265–290. http://dx.doi.org/10.1146/annurev.bb.16.060187.001405

Valentine, J.W., A.G. Collins, and C.P. Meyer. 1994. Morphological complexity increase in metazoans. *Paleobiology*. 20:131–142. http://dx.doi.org/10.1017/S0094837300012641

Wang, E.T., R. Sandberg, S. Luo, I. Khrebtukova, L. Zhang, C. Mayr, S.F. Kingsmore, G.P. Schroth, and C.B. Burge. 2008. Alternative isoform regulation in human tissue transcriptomes. *Nature*. 456:470–476. http://dx.doi.org/10.1038/nature07509

Weiss, N., and G.W. Zamponi. 2013. Control of low-threshold exocytosis by T-type calcium channels. *Biochimica et Biophysica Acta (BBA) - Biomembranes*. 1828:1579–1586. http://dx.doi.org/10.1016/j.bbamem.2012.07.031

Weiss, N., S. Hameed, J.M. Fernández-Fernández, K. Fablet, M. Karmazinova, C. Poillot, J. Proft, L. Chen, I. Bidaud, A. Monteil, et al. 2012. A $Ca_v3.2$/syntaxin-1A signaling complex controls T-type channel activity and low-threshold exocytosis. *J. Biol. Chem.* 287:2810–2818. http://dx.doi.org/10.1074/jbc.M111.290882

Yeoman, M.S., B.L. Brezden, and P.R. Benjamin. 1999. LVA and HVA Ca^{2+} currents in ventricular muscle cells of the *Lymnaea* heart. *J. Neurophysiol.* 82:2428–2440.

Yoon, T.-Y., X. Lu, J. Diao, S.-M. Lee, T. Ha, and Y.-K. Shin. 2008. Complexin and Ca^{2+} stimulate SNARE-mediated membrane fusion. *Nat. Struct. Mol. Biol.* 15:707–713. http://dx.doi.org/10.1038/nsmb.1446

Zhong, X., J.R. Liu, J.W. Kyle, D.A. Hanck, and W.S. Agnew. 2006. A profile of alternative RNA splicing and transcript variation of CACNA1H, a human T-channel gene candidate for idiopathic generalized epilepsies. *Hum. Mol. Genet.* 15:1497–1512. http://dx.doi.org/10.1093/hmg/ddl068